The Astrophysical Journal, 652:1374–1389, 2006 December 1
© 2006. The American Astronomical Society. All rights reserved. Printed in U.S.A.

THE ROTATING MOLECULAR CORE AND PRECESSING OUTFLOW OF THE YOUNG STELLAR OBJECT BARNARD 1c

Brenda C. Matthews
Herzberg Institute of Astrophysics, National Research Council of Canada, 5071 West Saanich Road, Victoria, BC, V9E 2E7, Canada; brenda.matthews@nrc-cnrc.gc.ca

Michiel R. Hogerheijde
Leiden Observatory, P.O. Box 9513, 2300 RA, Leiden, Netherlands; michiel@strw.leidenuniv.nl

Jes K. Jørgensen
Harvard-Smithsonian Center for Astrophysics, 60 Garden Street MS42, Cambridge, MA 02138; jjorgensen@cfa.harvard.edu

and

Edwin A. Bergin
Department of Astronomy, University of Michigan, 825 Dennison Building, 500 Church Street, Ann Arbor, MI 48109; ebergin@umich.edu
Received 2006 April 13; accepted 2006 August 24

ABSTRACT

We investigate the structure of the core surrounding the recently identified deeply embedded young stellar object Barnard 1c. B1c lies within the Perseus molecular cloud at a distance of 250 pc. It is a deeply embedded core of 2.4 $M_\odot$ (Kirk et al.) and a luminosity of $4 \pm 2\,L_\odot$. Observations (and resolutions) of ^{12}CO $J = 1-0$ ($9\farcs2 \times 5\farcs9$), ^{13}CO $J = 1-0$, C^{18}O $J = 1-0$ ($14\farcs3 \times 6\farcs7$), HCO$^+$ $J = 1-0$ ($7\farcs6 \times 5\farcs8$), and N_2H^+ $J = 1-0$ ($5\farcs9 \times 4\farcs6$) were obtained with the BIMA array, together with the continuum at 3.3 mm ($6\farcs4 \times 4\farcs9$) and 2.7 mm ($9\farcs5 \times 6\farcs3$). Single-dish measurements of N_2H^+ $J = 1-0$ and HCO$^+$ $J = 1-0$ with FCRAO reveal the larger scale emission in these lines with ~60 resolution. The ^{12}CO and HCO$^+$ emission traces the outflow extending over the full field of view ($2\farcm1$), which coincides in detail with the S-shaped jet recently found in *Spitzer* IRAC imaging. The N_2H^+ emission, which anticorrelates spatially with the C^{18}O emission, originates from a rotating envelope with effective radius ~2400 AU and mass 2.1–2.9 $M_\odot$, as derived from the 3.3 mm continuum emission. N_2H^+ emission is absent from a 600 AU diameter region around the young star, offset from the continuum peak. The remaining N_2H^+ emission may lie in a coherent torus of dense material. With its outflow and rotating envelope, B1c closely resembles the previously studied object L483 mm, and we conclude that it is a protostar in an early stage of evolution, i.e., Class 0 or in transition between Class 0 and Class I. We hypothesize that heating by the outflow and star has desorbed CO from grains, which has destroyed N_2H^+ in the inner region, and surmise that the presence of grains without ice mantles in this warm inner region can explain the unusual polarization signature observed from B1c.

Subject headings: ISM: clouds — ISM: molecules — ISM: individual (Barnard 1) — radio lines: ISM — stars: formation

1. INTRODUCTION

Class 0 sources represent the youngest phase of low-mass star formation. They are characterized by higher infall rates than more evolved sources based on outflow activity (Bontemps et al. 1996; Whitworth & Ward-Thompson 2001), an absence of optical emission, and a high ratio of submillimeter to bolometric luminosity. Observations of the internal structure of Class 0 objects rely on interferometers because the sources remain deeply embedded within their parent molecular clouds. To understand the kinematics of the collapse process requires observation of multiple molecular lines because the chemistry within these dense, cold cores is complex. Carbon-bearing species are observed to be strongly depleted within the core interiors due to freeze-out onto grains. Nitrogen-bearing species were thought to deplete much more slowly than carbon-bearing species because of the low binding energy of the N_2 molecule, requiring long periods of time or very high densities to show depletion (Bergin & Langer 1997; Bergin et al. 2002). However, recent laboratory results indicate that CO binding energies are comparable to those of N_2. These studies also indicate that the degree of mixing of N_2 and CO ices impacts the desorption timescales (Öberg et al. 2005; Bisschop et al. 2006). Nonetheless, it is clear that N_2H^+ (and its daughter product NH_3) show a strong rise in abundance as its main destroyer, ^{12}CO, depletes from the gas, making N_2H^+ an effective tracer of internal core kinematics (e.g., Aikawa et al. 2005). When ^{12}CO is present however, reactions between C$^+$ or ^{12}CO lead to the eventual destruction of the two standard nitrogen-bearing tracers: NH_3 and N_2H^+.

Recent observations of several Class 0 sources have shown an absence of N_2H^+ emission at the source position on scales within several hundred AU of the protostar (i.e., Jørgensen et al. 2004b). Typically, N_2H^+ emission is depressed at the core center and has been interpreted as destruction of N_2H^+ due to evaporation of CO and its isotopes from dust grains (e.g., L483 mm, hereafter L483; Jørgensen 2004) or depletion of N_2H^+ at high densities (e.g., IRAM 04191+1522, hereafter IRAM 04191; Belloche et al. 2002). An absence of N_2H^+ cannot be purely an indicator of age; L483 is thought to be in transition between Class 0 and Class I (Tafalla et al. 2000) while IRAM 04191 is estimated to be among the youngest Class 0 sources known (André et al. 1999). Interestingly, in both cases, the N_2H^+ emission morphology is double peaked around the source center with a signature indicating rotation, and an anticorrelation is noted between N_2H^+ emission and the emission from tracers dominated by the outflow (^{12}CO and HCO$^+$).

However, in L483, $C^{18}O$ is centrally peaked on the source, indicating that ^{12}CO has been evaporated from dust grains at the core center. The combination of N_2H^+ and $C^{18}O$ morphology could thus discriminate between whether an absence of N_2H^+ is due to depletion onto dust grains or the destruction of N_2H^+ in the presence of ^{12}CO.

In this paper we present observations of the internal structure of the protostellar core Barnard 1c (B1c) from the Berkeley-Illinois-Maryland Association (BIMA) array and the Five Colleges Astronomical Radio Observatory (FCRAO) 14 m telescope. B1c was discovered during 850 μm polarimetry mapping in Barnard 1 by Matthews & Wilson (2002). Recent IRAC imaging from *Spitzer* reveals that this source is highly reddened and deeply embedded in the B1 cloud with an extensive, highly collimated outflow (Jørgensen et al. 2006). The presence of central cavities within young protostellar cores is of particular relevance to B1c because a heated central region could explain why B1c has a unique signature in polarized emission. Its polarization pattern suggests that the polarized intensity rises to the center of the core (Matthews & Wilson 2002), rather than flattening out as seen in other cores. When compared to the total intensity, a flat distribution in polarized intensity produces a declining ratio toward the peaks of cores. All other low-mass starless and star-forming cores observed in polarized dust emission have a so-called polarization hole at high intensities, thought to arise from changes in magnetic field geometry or dust grain physics (Matthews 2005). One of the favored explanations for the polarization holes is that the grains at core centers are ineffective polarizers (due to changing grain physics). Heating removes the outer grain mantles and could increase the polarization efficiency of the grains within cavities (Whittet et al. 2001).

Barnard 1 is part of the Perseus molecular cloud complex (Bachiller & Cernicharo 1986) which is one of the closest star-forming regions to the Sun. Its distance is the subject of some debate, with estimates ranging from 200 pc (based on extinction studies; Černis 1990) to 330–350 pc (based on the Per OB2 association; de Zeeuw et al. 1999; Borgman & Blaauw 1964; Herbig & Jones 1983). It has been suggested that the complex may be composed of two clouds at 200 and 300 pc (Cernicharo et al. 1985), that there is a distance gradient along its length (Sargent 1979), or that it is comprised of independent clouds at varying distances (Ridge et al. 2006). To facilitate comparison with recent works on the Perseus cloud (i.e., Enoch et al. 2006; Jørgensen et al. 2006), we adopt a distance of 250 $\pm$ 50 pc to the Barnard 1 cloud, as determined from recent estimates of extinction (Černis & Straizys 2003) and measurements of parallax in members of IC 348 (Belikov et al. 2002).

This paper presents high-resolution interferometric data from several molecular species and continuum emission at 2.7 and 3.3 mm. The main objective is to determine whether B1c exhibits a central cavity which could help explain its unique polarization properties. The observations and data reduction techniques are described in § 2. We present the continuum results and derive the core mass in § 3. The molecular line data are presented in § 4. We discuss these data in § 5. Our findings are summarized in § 6.

2. OBSERVATIONS AND DATA REDUCTION

2.1. *BIMA Interferometric Data*

Observations were made over the period of 2002 October to 2003 April using the BIMA interferometer (Welch et al. 1996) in Hat Creek, California. We utilized a single pointing toward the position $\alpha = 03^h33^m17^s.8$, $\delta = +31^\circ09'33''.0$ (J2000.0). Two configurations of the 10 6.1 m antennas were used to observe the lines of N_2H^+ $J = 1-0$ and HCO^+ $J = 1-0$. The C and B arrays had projected baselines between 2–33 and 3–74 kλ, respectively. The ^{12}CO $J = 1-0$ line and its isotopomers ^{13}CO $J = 1-0$ and $C^{18}O$ $J = 1-0$ were observed only in the C-array configuration. Table 1 contains the sensitivities achieved per track.

The N_2H^+ $J = 1-0$ line was observed utilizing the digital correlator to record the line in bands of 6.25 and 12.5 MHz width with 256 channels each, giving resolutions of 0.079 and 0.157 km s^{-1}. The larger bandwidth window permitted detections over the range of the seven hyperfine components of N_2H^+ $J = 1-0$. All 10 antennas were available for both 93 GHz tracks.

The HCO^+ $J = 1-0$ line was observed in bandwidths of 6.25 and 12.5 MHz with 256 channels each, resulting in resolutions of 0.082 and 0.164 km s^{-1}, respectively. A window in the upper side band was sensitive to SiO $J = 2-1$ in a 12.5 MHz window with 0.085 km s^{-1} resolution. Three tracks were obtained in the B array and two in the C array. All 10 antennas were available for three tracks, with one antenna offline for a B array track and two antennas missing from one of the C array tracks.

The ^{12}CO $J = 1-0$ line was observed in a band 12.5 MHz wide across 256 channels. We also observed it in 100 MHz windows to detect high-velocity CO gas. The velocity resolutions were 0.127 and 8.127 km s^{-1}, respectively. No CO emission was detected at velocities exceeding 20 km s^{-1} from the rest velocity of the source. As for the N_2H^+ $J = 1-0$ data set, the phase calibrators were 3C 84 and 0237+288. Only 9 of 10 antennas were usable for this track due to phase incoherence on antenna 9. We were sensitive to the CN $J = 1-0$ line in the USB during this observation, but none was detected.

The ^{13}CO $J = 1-0$ and $C^{18}O$ $J = 1-0$ lines were observed with the digital correlator configured to record the lines in the upper side band with 12.5 MHz bandwidth over 256 channels. One antenna was offline during this track. Data from a second antenna was flagged due to the same phase problems. Spectral line data from a third antenna was removed due to noisy phases and amplitudes.

Phase and amplitude variations were calibrated by observing the nearby quasars 3C 84 and 0237+288 (when 3C 84 reached elevations exceeding 85°) approximately every 30 minutes. The adopted fluxes of these quasars was epoch dependent and measured against observations of the planet Uranus when possible. The calibration was performed using the MIRIAD (Multichannel Image Reconstruction, Image Analysis and Display; Sault et al. 1995) task MSELFCAL. Absolute flux calibration was done using Uranus when observed or by derived fluxes of the gain calibrators during the same epoch as our observations (utilizing the catalog of fluxes at `plot_swflux` on the BIMA World Wide Web site[1]). Based on the uncertainty in flux of the calibrator and the relative variations in the flux of the quasar, we estimate our overall flux calibration is accurate to the 30% level.

Subsequent processing of the data, including the combination of data from different configurations, were done with MIRIAD. Images were produced using MIRIAD's CLEAN algorithm and "robust" weighting (robustness parameter 0–2) of the visibilities to optimize the signal-to-noise ratio (S/N) and the spatial resolution. Resulting noise levels are 0.15 Jy beam^{-1} in 0.16 km s^{-1} channels for the N_2H^+ $J = 1-0$ and HCO^+ $J = 1-0$ line emission, 0.4, 0.6, and 1.0 Jy beam^{-1} in 0.13 km s^{-1} channels for the ^{13}CO $J = 1-0$, $C^{18}O$ $J = 1-0$, and ^{12}CO $J = 1-0$ line emission, respectively. The rms levels in the continuum maps are 6.8 and 4.1 mJy beam^{-1} for the continuum images at 2.7 and 3 mm, respectively. The best naturally weighted resolution is obtained

[1] See http://bima.astro.umd.edu.

TABLE 1
Observational Summary of Molecular Species

Transition	Frequency (GHz)	Date	Array Configuration	Resolution (km s^{-1})	Sensitivity (Jy beam^{-1})
N_2H^+ $J = 1-0$	93.17378	2002 Nov 19	C	0.079	0.4
				0.157	0.28
		2003 Feb 27	B	0.079	0.32
				0.157	0.21
HCO^+ $J = 1-0$	89.18852	2002 Oct 24	C	0.082	0.4
				0.164	0.27
		2003 Jan 25	B	0.082	1.3
				0.164	0.9
		2003 Mar 11	B	0.082	1.1
				0.164	0.75
		2003 Mar 16	B	0.082	0.6
				0.164	0.4
		2003 Apr 7	C	0.082	0.38
				0.164	0.26
SiO $J = 2-1$[a]	85.64046	2002 Oct 24	C	0.085	0.38
		2003 Jan 25	B	0.085	1.4
		2003 Mar 11	B	0.085	1.0
		2003 Mar 16	B	0.085	0.5
		2003 Apr 7	C	0.085	0.37
^{12}CO $J = 1-0$	115.21720	2002 Dec 4	C	0.127	1.4
^{13}CO $J = 1-0$	110.20135	2002 Nov 20	C	0.066	0.65
				0.133	0.45
$C^{18}O$ $J = 1-0$	109.78217	2002 Nov 20	C	0.067	0.67
				0.133	0.48

[a] Not detected.

for N_2H^+ $J = 1-0$, with a beam of FWHM of $5\farcs9 \times 4\farcs6$. Moderate resolution is obtained for HCO^+ $J = 1-0$ and ^{12}CO $J = 1-0$ with FWHM of $7\farcs6 \times 5\farcs8$ and $9\farcs2 \times 5\farcs9$, respectively. Due to limited (u, v) coverage, the FWHM of ^{13}CO $J = 1-0$ and $C^{18}O$ $J = 1-0$ data is $14\farcs3 \times 6\farcs7$. Integrated-intensity and velocity-centroid images were obtained from the cleaned spectral-line cubes using a 1 or 2 σ clip level. The resolution of the continuum images is $9\farcs5 \times 6\farcs3$ and $6\farcs4 \times 4\farcs9$ for 2.7 and 3.3 mm, respectively.

2.2. *FCRAO Data*

To obtain information on large spatial scales, we observed B1c in N_2H^+ $J = 1-0$ and HCO^+ $J = 1-0$ emission with the FCRAO. The data were obtained in very good weather. We achieved an rms of 0.08 K (T_A^*) in 24 minutes on source. The N_2H^+ $J = 1-0$ and HCO^+ $J = 1-0$ data were obtained simultaneously using the array SEQUOIA. The beam size of the FCRAO data is $57\farcs5$ at 93.17378 GHz and $60\farcs5$ at 89.188523 GHz. The maps cover an area of diameter $12\farcm5$ centered on the continuum peak of the BIMA array data.

2.3. *Combination of Single-Dish and Interferometer Data*

For the HCO^+ and N_2H^+ data sets, we were able to combine the BIMA array and FCRAO data to obtain total power maps of each transition. We utilized the method described by Stanimirovic et al. (1999) to combine the data in the image plane.

The FCRAO data were reordered to match the BIMA axes (x, y, v), converted to main beam from antenna temperature, and rescaled to Janskys. The MIRIAD task REGRID was then used to regrid the FCRAO data to match the parameters of the BIMA array data cube. Slight differences in line frequencies were compensated for by a shift in the reference velocity of the FCRAO spectra prior to regridding. The shifts required were 0.885 and 0.016 km s^{-1} for N_2H^+ $J = 1-0$ and HCO^+ $J = 1-0$ spectra, respectively. In the latter case, the shift is significantly less than the width of individual channels. A map of the FCRAO beam for each transition was generated and truncated at the 5% level, creating a mask applied to the appropriate single-dish data cube. The weighting factor for the single-dish map was determined by a ratio of the beam areas. The composite map was then created using a linear combination of the BIMA dirty map and the single-dish map, followed by deconvolution using the combined beam (Stanimirovic et al. 1999).

3. DUST EMISSION TOWARD B1c

Figure 1 shows the continuum detections toward B1c at 3.3 and 2.7 mm. The source is located at $\alpha = 03^h33^m17\fs878$, $\delta = +31^\circ09'31\farcs98$ (J2000.0), which is the peak of the 3.3 mm emission. The 2.7 mm emission is poorly resolved with positive flux density detected to a radius of $13''$. The 3.3 mm emission is better resolved with the core extending to $11''$.

The continuum emission is not pointlike; Figure 1 shows that it is extended to the northwest and the southeast of the continuum peak at both wavelengths. The continuum emission to the southeast does not coincide at the two wavelengths, but in each case it is strong, exceeding 4 σ at 3.3 mm at $\alpha = 03^h33^m18\fs75$, $\delta = +31^\circ09'21\farcs1$, corresponding to 16.6 mJy beam^{-1}. The 2.7 mm peak to the southeast also exceeds 3 σ (21.7 mJy beam^{-1}) at $\alpha = 03^h33^m20\fs20$, $\delta = +31^\circ09'14\farcs5$.

Figure 2 shows the visibility amplitude as a function of (u, v) distance at each wavelength. Flux detections above the zero-sigma value (*dashed lines*) are found for only a few of the shortest (u, v) distances and are generally marginal detections. Based on these plots, we interpret the continuum maps as spatially filtered observations of a resolved, extended envelope, similar to the case of L483 (see Fig. 2 of Jørgensen 2004). The poorer (u, v) sampling at 2.7 mm leads to the recovery of less extended emission than we detect at 3.3 mm.

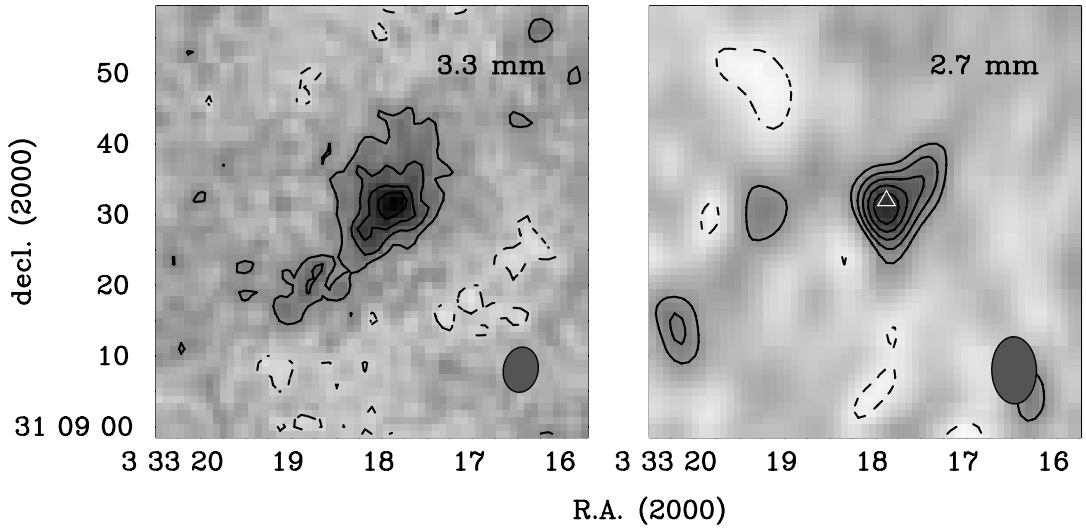

FIG. 1.—Continuum emission from B1c at 3.3 and 2.7 mm. The respective beams are shown at the bottom right. The 3.3 mm contours are plotted at 2, 4, 6, and 8 σ, where $\sigma = 4.1$ mJy beam^{-1}. The 2.7 mm contours are at levels of 2, 3, 4, 5, and 6 σ, where $\sigma = 6.8$ mJy beam^{-1}.

Using the MIRIAD task IMFIT, we have fit Gaussians to the 2.7 and 3.3 mm maps, fixing the peak flux density and position of the peak emission. As Table 2 shows, the resultant total flux densities derived are higher than those obtained by use of aperture photometry. As expected from Figure 2, less flux is recovered at 2.7 mm than at 3.3 mm. However, the sizes measured for the core are remarkably similar at each wavelength. Based on the 3.3 mm deconvolved size, the scale of the detected inner envelope is $\sim$3100 AU $\times$ 1800 AU at 250 pc. The effective radius of this central region ($r_{\rm eff} = \sqrt{ab}$, where a and b are the major and minor axes, respectively) is $\sim$2400 AU. This is much smaller than the 12000 AU effective radius derived from the SCUBA map at 850 μm by Kirk et al. (2006). The measurement from the JCMT (James Clerk Maxwell Telescope) incorporates the entire outer envelope of B1c, to which our BIMA array data are not sensitive. It is normal to measure less flux in interferometric maps than in single-dish data because interferometers preferentially sample structure on small scales. Therefore, our continuum estimates only apply to the inner envelope (i.e., not the region traced by the JCMT).

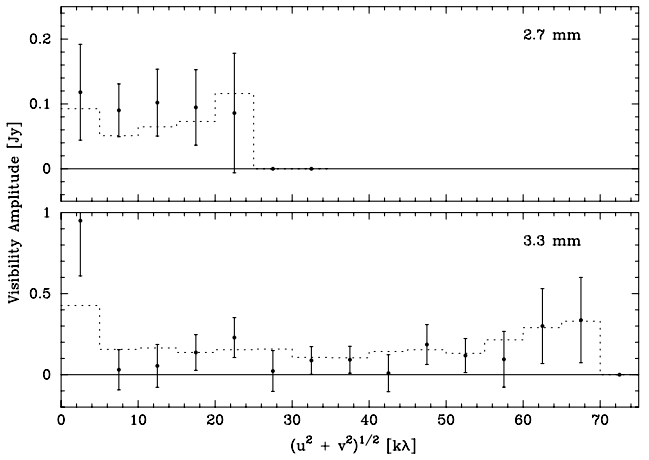

FIG. 2.—Plots of visibility amplitude vs. projected baseline for our continuum data sets. Points are the amplitudes; the error bars are the formal standard deviations from the mean. The dotted line represents the signal expected from the noise. We have only a single track each at 109 and 115 GHz, both in the C array. This is reflected in the extremely limited (u, v) distance coverage. Those bins where the detected amplitude exceeds the value consistent with noise are even more limited. The coverage is much better at 3.3 mm, where we have multiple tracks at 89 and 93 GHz, in both the B and C arrays. Similarly, the range of projected baselines in which we detect signal well above those consistent with noise are also much more extended.

At 3.3 mm, it is possible that some continuum emission may be due to free-free emission instead of emission from dust. We have reduced an archival observation[2] from the Very Large Array at 1.3 cm in which B1c lies just outside the primary beam. There is no detection of 1.3 cm emission in this map, and the 3 σ upper limit is 3.7 mJy beam^{-1}. Since the free-free emission is expected to be relatively flat, a contribution of this magnitude cannot be a significant source of the continuum emission at 3.3 mm.

3.1. *Mass, Column, and Density of the Inner Core*

The mass of the continuum source is easily determined, assuming optically thin conditions, from the flux of the source and the temperature via the relation

$$M = \frac{F_\nu d^2}{\kappa_\nu B_\nu(T_d)}, \quad (1)$$

where F_ν is the flux, d is the source distance, κ_ν is the dust opacity and $B_\nu(T_d)$ is the Planck function at temperature T_d. Table 3

[2] The National Radio Astronomy Observatory is a facility of the National Science Foundation operated under cooperative agreement by Associated Universities, Inc.

TABLE 2
CONTINUUM RESULTS

Parameter	2.7 mm	3.3 mm
Measured peak flux density (mJy beam^{-1})	47.5 ± 14	39.0 ± 13
Total flux density:		
Aperture (mJy)[a]	71 ± 21	123 ± 37
Gaussian fit (mJy)	89 ± 27	150 ± 50
Size (arcsec)	12.5 × 8.9	13.8 × 8.8
P.A. (deg)	−51	−30
Deconvolved size (arcsec)	10.2 × 1.6	12.3 × 7.2
Deconvolved P.A. (deg)	−66	−33

[a] Measured in apertures of 13″ and 11″ radius for 2.7 and 3.3 mm, respectively.

TABLE 3
Masses and Column Densities from Continuum Flux Density

Parameter	2.7 mm		3.3 mm	
	$\beta = 1$	$\beta = 1.5$	$\beta = 1$	$\beta = 1.5$
[a] κ_ν (cm^2 g^{-1})	0.0049	0.0034	0.0039	0.0025
Mass:				
T_d = 12 K ($M_\odot$)	1.2 ± 0.4	1.73 ± 0.5	3.71 ± 1.1	5.91 ± 1.8
T_d = 15 K ($M_\odot$)	0.92 ± 0.3	1.32 ± 0.4	2.86 ± 0.9	4.55 ± 1.4
T_d = 20 K ($M_\odot$)	0.66 ± 0.2	0.94 ± 0.3	2.06 ± 0.6	3.29 ± 1.0
Column density:				
T_d = 12 K (10^{23} cm^{-2})	4.3 ± 1.3	6.2 ± 1.9	12 ± 4	20 ± 6
T_d = 15 K (10^{23} cm^{-2})	3.3 ± 1.1	4.7 ± 1.4	9.5 ± 2.9	15 ± 5
T_d = 20 K (10^{23} cm^{-2})	2.4 ± 0.7	3.4 ± 1.0	6.8 ± 2.0	1.1 ± 0.3

[a] Derived from $\kappa_\nu = \kappa_0(\nu/\nu_0)^\beta$ where κ_0 is calculated to be 0.01 cm^2 g^{-1} at $\nu_0 = 231$ GHz (Ossenkopf & Henning 1994).

presents the masses calculated for our measured flux densities for different assumptions of β (and hence κ_ν) and T_d. Our continuum maps are spatially filtered and are not sensitive to the large-scale emission of the core (i.e., the outer envelope). If this source is young, then much of the mass is expected to remain in the envelope; therefore, observations sensitive only to the inner envelope should be expected to yields masses smaller than that measured with a single-dish telescope.

Kirk et al. (2006) derive a mass of 2.4 $M_\odot$ for B1c based on SCUBA observations at 850 μm. The clump size ($R_{\rm eff} = 49''$) and mass were measured with CLUMPFIND (Williams et al. 1994). This estimate of mass and size includes the entire outer envelope, and we note that the size scale exceeds the maximum scale to which our BIMA array data are sensitive: 1.′1 at 2.7 mm and 1.′3 at 3.3 mm. We concentrate our discussion on the 3.3 mm emission since, as discussed above, our flux recovery is better at that wavelength. The requirement that the interferometric mass estimate be less than the single-dish mass estimate allows us to put some constraints on β and T_d. The dust temperature is $\geq$15 K and β is more likely to be closer to 1.0 than to 1.5. For the same dust temperature as derived from single-dish data (15 K) and $\beta = 1.0$, the mass of the inner envelope is 2.9 ± 0.9 $M_\odot$. For $T_d = 20$ K, the mass is 2.1 ± 0.6 $M_\odot$. Therefore, the mass of the inner core lies in the range 2.1–2.9 $M_\odot$.

Here, we reiterate that our continuum data are hindered by excessive spatial filtering. This caveat prevents us from rigorously predicting values of β or dust temperature in the inner core, since the BIMA flux densities are not easily compared either to each other or the existing single-dish flux density from the JCMT.

Using the continuum flux, we can also estimate the column density of molecular hydrogen within the core using the relation:

$$N(\mathrm{H_2}) = \frac{S_\nu}{\Omega_m \mu m_{\rm H} \kappa_\nu B_\nu(T_d)}, \quad (2)$$

where S_ν is the peak flux density, Ω_m is the main-beam solid angle in steradians, μ is the mean molecular weight (2.33), $m_{\rm H}$ is the mass of atomic hydrogen, κ_ν is the dust opacity per unit mass. Table 3 contains estimates of the column density for different values of β and T_d. At 3.3 mm, for a temperature of 20 K, the column density toward the peak is (6.8 ± 2.0) × 10^{23} cm^{-2}, for β = 1.0. Conversion to extinction using $N(\mathrm{H_2})/A_V = 10^{21}$ cm^2/mag yields a visual extinction of 680 ± 200 mag to the central peak of the B1c core.

Assuming that the inner envelope is as deep as it is wide, we can crudely estimate the central density by adopting the effective diameter as the depth and assuming a constant density sphere. Then the density is just the column density divided by the depth, and the central column density is ∼(9.0 ± 2.6) × 10^6 cm^{-3}. A comparable calculation using 2.7 mm data yields the lower estimate of (3.3 ± 1.0) × 10^6 cm^{-3}. Reasonable estimates of the density therefore range from (3–9) × 10^6 cm^{-3}.

4. MOLECULAR EMISSION TOWARD B1c

Maps of the integrated intensity of ^{12}CO $J = 1-0$, ^{13}CO $J = 1-0$, C^{18}O $J = 1-0$, HCO$^+$ $J = 1-0$, N_2H^+ $J = 1-0$, and SiO $J = 2-1$ as detected by the BIMA array are presented in Figure 3. The outflow from B1c is prominently detected in ^{12}CO $J = 1-0$ and HCO$^+$ $J = 1-0$. The N_2H^+ $J = 1-0$, and C^{18}O $J = 1-0$ clearly trace the envelope around the central source. The ^{13}CO $J = 1-0$ detections show no emission associated with the core, but may trace some compact features in the outflow. SiO $J = 2-1$ is not detected. The systematic velocity of the source is 6.35 ± 0.02 km s^{-1}, based on a fit to the N_2H^+ $J = 1-0$ spectrum at the position of the continuum source.

4.1. *The Core in* N_2H^+ *and* C^{18}O

N_2H^+ $J = 1-0$ is strongly detected in B1c, indicating dense, cold gas within the core. Figure 3*a* shows that the integrated intensity of N_2H^+ $J = 1-0$ exhibits a double-peaked structure, with both peaks avoiding the position of the continuum source (*triangle*) and the outflow, as shown in Figures 3*d* and 3*e*. In contrast, Figure 3*b* shows that the C^{18}O $J = 1-0$ emission is strongly centrally peaked very close to the continuum source position. Figure 4 shows a comparison of the distributions of the C^{18}O and N_2H^+ emission. The emission in a strip along the flattened axis of the core is also shown. This figure clearly illustrates the relative positions of the peaks in the C^{18}O $J = 1-0$ and N_2H^+ $J = 1-0$ emission. Despite our significantly poorer resolution in C^{18}O $J = 1-0$, the distribution is strikingly similar to that observed toward the more luminous (9 $M_\odot$) evolved Class 0 source L483 (Fig. 10 of Jørgensen 2004). The relative strength of the emission at each N_2H^+ peak is comparable, which differs from the results in L483, in which one peak was noticably brighter than the other.

This morphology is seen across a wide range of young protostellar objects. For example, it is also observed in NGC 1333 IRAS 2 (Jørgensen et al. 2004a) and sources in the Serpens molecular cloud (Hogerheijde 2005). It is also noted in the very low luminosity object (VeLLO) IRAM 04191 (0.15 $L_\odot$; Lee et al. 2005). In B1c, the N_2H^+ emission is not confined merely

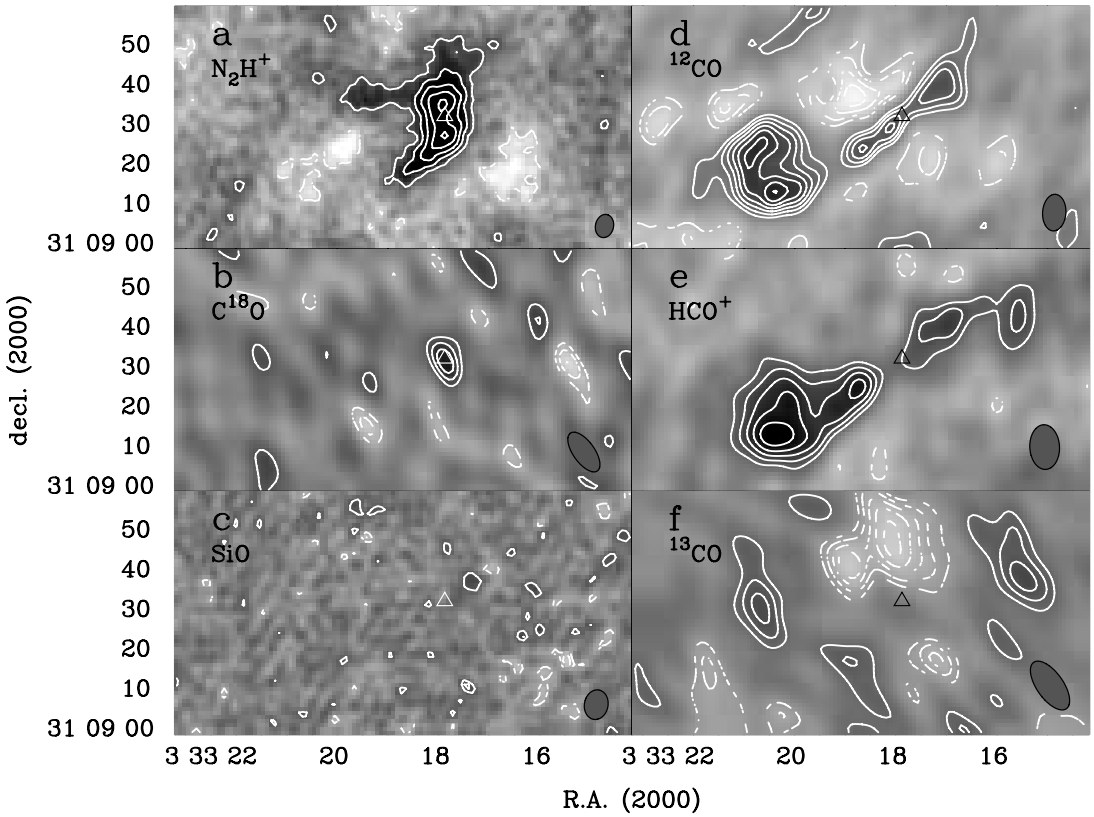

FIG. 3.—Maps of integrated intensity in ^{12}CO $J = 1-0$, ^{13}CO $J = 1-0$, $C^{18}O$ $J = 1-0$, HCO^+ $J = 1-0$, N_2H^+ $J = 1-0$, and SiO $J = 2-1$ toward the source Barnard 1c. (*a*) N_2H^+ $J = 1-0$ map shows the double-peaked distribution with peaks offset from the 3.3 mm continuum peak of Fig. 1, shown as a triangle. The N_2H^+ data are integrated over 21.2 km s^{-1} (a range that contains all seven hyperfine components); contours range from 2 to 10 σ in steps of 2 σ, where $\sigma = 47$ mJy beam^{-1}. Dashed contours show the corresponding negative contours. (*b*) $C^{18}O$ $J = 1-0$ data clearly trace the core emission and are centrally peaked on the 3.3 mm continuum source peak (*triangle*). The $C^{18}O$ data are uniform weighted for better resolution ($11\farcs7 \times 5\farcs4$) and integrated over 2.1 km s^{-1}, and the contours range from 2 to 4 σ in steps of 1 $\sigma = 0.17$ Jy beam^{-1}. (*c*) SiO $J = 2-1$ data shows no significant detections. Contour levels are 2 and 3 σ, where $\sigma = 0.03$ Jy beam^{-1}. (*d*) ^{12}CO $J = 1-0$ integrated intensity in gray scale and white contours; contours range from 2 to 8 σ, where $\sigma = 0.16$ Jy beam^{-1}. Negative contours of the same range are also plotted. The ^{12}CO map is integrated over 12.7 km s^{-1}. (*e*) HCO^+ map in gray scale and white contours; data are integrated over 17.2 km s^{-1}. The contours range from 2 to 6 σ, where $\sigma = 35$ mJy beam^{-1}. (*f*) ^{13}CO $J = 1-0$ integrated emission over 4.3 km s^{-1} reveals no emission associated with the continuum peak (*triangle*). Contours range from 2 to 4 σ in steps of 1 $\sigma = 75$ mJy beam^{-1}. As in other plots, the dashed contours represent corresponding negative values.

to the two peaks, but extensions are detected to the east and southeast that bound the outflow emission in ^{12}CO and HCO^+. These extensions could be the dense edges of a conical cavity carved into the envelope by the molecular outflow, as depicted in our schematic diagram of the source (see Fig. 5). The projected opening angle of this cavity is $\sim 55^\circ$, based on the lowest contour of the eastern extensions of N_2H^+ emission in the integrated intensity images (Fig. 3*a*) relative to the position of the continuum source. The uncertainty on the opening angle of the cavity is $\sim 10^\circ$. A third extension in N_2H^+ is observed to the northwest along the 3 σ contours of the HCO^+ and CO emission. No N_2H^+ is detected along the other edge of the redshifted outflow emission in the integrated intensity map.

4.2. *The Outflow in* HCO^+ *and* ^{12}CO

The molecular outflow is clearly seen in both ^{12}CO $J = 1-0$ and HCO^+ $J = 1-0$, as shown in Figures 3*d* and 3*e*. We did not detect any SiO $J = 2-1$ emission as shown by Figure 3*c*. The detected ^{12}CO $J = 1-0$ and HCO^+ $J = 1-0$ emission exhibits a bipolar morphology with the blue lobe emission to the southeast much stronger than the red lobe emission to the northwest. Significantly, some ^{12}CO $J = 1-0$ emission is also detected coincident with the central core, but HCO^+ $J = 1-0$ is not detected toward the position of the continuum source. As observed in L483 by Jørgensen et al. (2004a). the N_2H^+ data is anticorrelated with the HCO^+ emission.

The zeroth moment of ^{12}CO and $C^{18}O$ data are compared in Figure 6. The $C^{18}O$ $J = 1-0$ emission is highly centrally peaked on the continuum source and is absent along the outflow axis, due to its relatively low abundance. The ^{12}CO $J = 1-0$ outflow appears to have carved out the lower density envelope traced by $C^{18}O$ $J = 1-0$ (integrated over the central velocities associated with the source) in a similar manner as the very dense gas traced by N_2H^+ $J = 1-0$ in Figure 3*a*. In fact, the optically thin species $C^{18}O$ $J = 1-0$ traces well both the continuum peak and small-scale structure within the inner envelope, detected on the edge of the ^{12}CO $J = 1-0$ emission along both the blue and red lobes. This is consistent with the findings of Arce & Sargent (2006) in their survey of outflow sources with the Caltech Millimeter Array. The orientation of the outflow from B1c is approximately -55° east of north. Based on the blue lobe, the opening angle appears to be $\sim 35^\circ$ in projection. Figure 6 also clearly indicates the presence of redshifted CO emission at the leading edge of the blue lobe.

4.2.1. *Spitzer Mid-Infrared Emission*

Figure 7 shows the outflow emission from the source B1c as imaged by *Spitzer* with IRAC at 4.5 μm (Jørgensen et al. 2006)

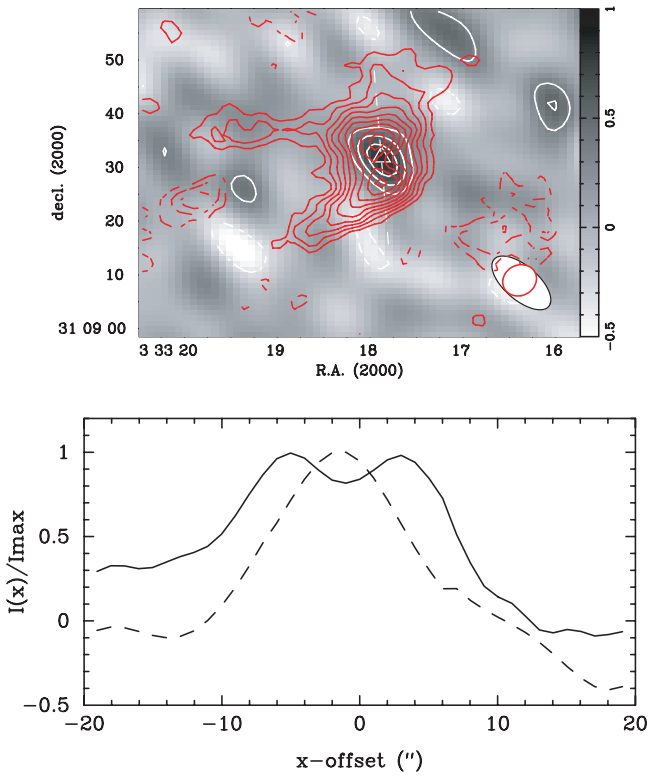

FIG. 4.—Comparison between N_2H^+ and $C^{18}O$ emission toward B1c. *Top panel:* The integrated N_2H^+ (*red contours*) and $C^{18}O$ (*gray scale and white contours*) emission. The flattened direction of the core is nearly north-south and is indicated by the dashed line. The beams are denoted at the lower right. *Bottom panel:* The N_2H^+ (*solid line*) and $C^{18}O$ (*dashed line*) emission along a slice denoted by the dashed line in the top panel. The anticorrelation between the peaks is evident. The ordinate value is the ratio of the flux density at the position along the slice relative to the peak flux density in the field.

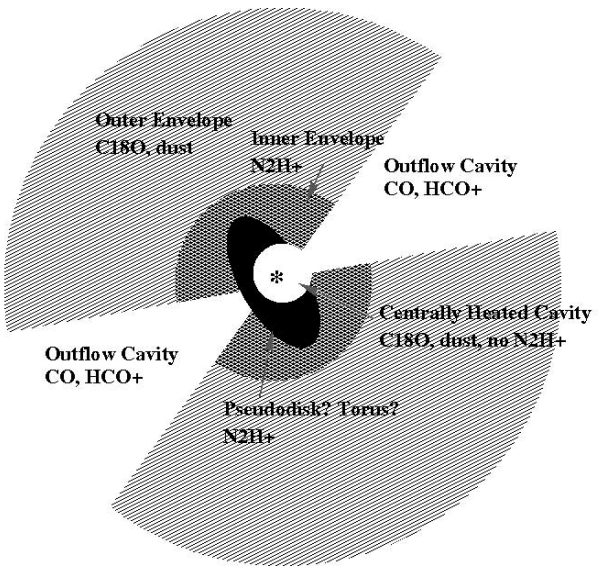

FIG. 5.—Schematic representation of the main features of the B1c source. Our interferometric data are insensitive to the large-scale outer envelope. We detect dense material from the inner envelope in N_2H^+ emission, some of which may be confined in a rotating torus centered on the source. The outflow, detected in ^{12}CO and HCO^+ has carved cavities in the inner (and presumably outer) envelope. A centrally heated cavity is indicated by the anticorrelation of $C^{18}O$ and N_2H^+ at the core center. Dust emission remains centrally peaked on the protostar because very high temperatures (2000 K) are required for its destruction.

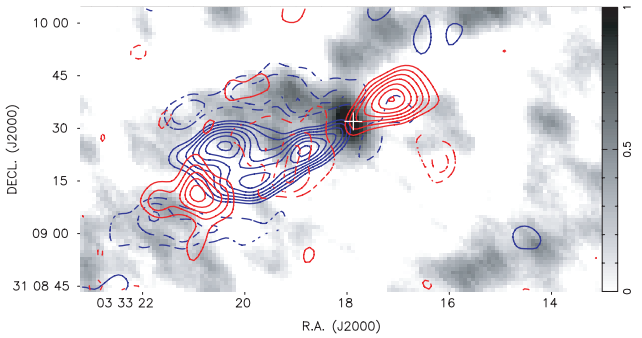

FIG. 6.—Moment 0 data for the red and blue CO outflow lobes toward B1c. The gray scale is $C^{18}O$ $J = 1–0$ emission from the core; the blue contours indicate blueshifted emission (2.4–5.1 km s^{-1}) and the red contours are the redshifted emission (8.4–13.8 km s^{-1}). Some redshifted emission is detected to the southeast of the blue lobe, indicating that the back of the conical cavity is being detected, or that the outflow is shifting direction at this location.

and the ^{12}CO outflow emission from the BIMA array. The IRAC 4.5 μm band has been found to be a strong tracer of outflows which is likely due to the presence of H_2 pure rotational transitions and the CO fundamental vibrational mode within the bandpass (Noriega-Crespo et al. 2004). The outflow clearly extends for several arcminutes on either side of the driving source, B1c. An "S-shaped" morphology is evident in the *Spitzer* map. Such S-shaped jets are interpreted as precession of the jet because of the presence of an (unseen) binary (e.g., Hodapp et al. 2005). Near the source, the outflow appears quite symmetric; however, at larger distances, the blue lobe widens while the red lobe appears to either split into two separate sequences of "bullets" or be confused with an outflow from a different source. The projected linear extent of the outflow detected by *Spitzer* is dependent on which distance one adopts to the Barnard 1 cloud. At 250 pc, the 6′ extent of the blue lobe from the central source indicates a distance of ~90,000 AU, or 0.44 pc.

Comparison of the *Spitzer* data with the BIMA array data illustrates that the 4.5 μm emission lies along the central axis of the CO outflow very near the driving source. Like the molecular hydrogen emission, there is a bend in the ^{12}CO emission, located precisely where the CO emission transitions from blueshifted to redshifted emission. We are constrained by the single pointing of

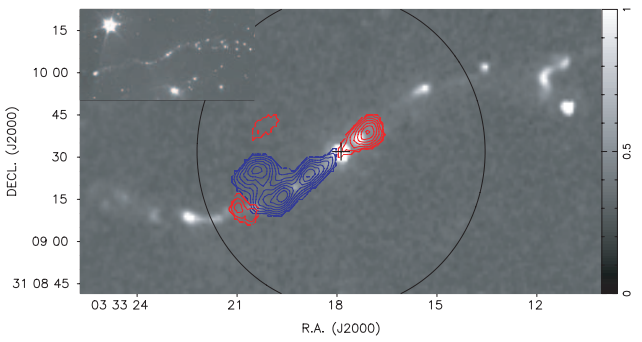

FIG. 7.—IRAC *Spitzer* data at 4.5 μm from Jørgensen et al. (2006) are compared to moment maps of the ^{12}CO $J = 1–0$ emission over the blue and red lobes. The correlation between the position angle and central axis of the outflow is excellent between the near-IR and millimeter data. The inset shows the larger scale extent of the molecular hydrogen emission seen from *Spitzer*. ^{12}CO $J = 1–0$ contours are from 3–10 Jy $beam^{-1}$ km s^{-1}, in steps of 1 Jy $beam^{-1}$ km s^{-1}. The cross marks the continuum peak of the BIMA data. The large circle indicates primary beam of a BIMA antenna.

the BIMA observations to a single primary beam of coverage in the CO emission. More extended ^{12}CO $J = 1-0$ measurements are needed to compare the morphology of the molecular hydrogen (the driving jet) to the morphology of the entrained gas mapped by the ^{12}CO. It is interesting that the position of the *Spitzer* emission peaks are anticorrelated with the CO peaks in the BIMA data, which is likely due to the difference in excitation conditions between the H_2 transitions that sample warm (few hundred K) gas along the jet shocks and ^{12}CO $J = 1-0$ which preferentially traces entrained, cold ($\sim$10 K) gas.

4.3. ^{13}CO $J = 1-0$ *Emission*

Figure 3*f* shows the integrated emission detected from ^{13}CO $J = 1-0$. In contrast to the other CO isotopologues, the ^{13}CO data do not clearly trace the core or the outflow. This is likely due to missing short spacings in the interferometric map which limit the sensitivity of this observation both to structure and emission. The peaks detected in ^{13}CO may be associated with the outflow or the walls of a cavity carved by the outflow.

4.4. *Moment Maps of the Core and Outflow*

We produced moment maps of the combined N_2H^+ $J = 1-0$ emission from the FCRAO and BIMA array data sets over a velocity range of 1.57 km s^{-1}, or 10 channels. After creating the moment maps, we masked out all data values in the moment 0 and moment 1 maps at positions with values less than 0.24 Jy beam^{-1} km s^{-1} in the moment 0 map, which is approximately 1.5 times the rms level per channel, 0.14 Jy beam^{-1}.

Figure 8 shows the first (*gray scale*) and zeroth (*contours*) moments of the combined N_2H^+ $J = 1-0$ emission. The velocity gradient suggests that the molecular core is rotating about an axis aligned with the outflow. As in the integrated intensity map from the BIMA array of Figure 3*a*, the zeroth-moment map of the combined data set illustrates a double-peaked distribution with peaks offset from the position of the continuum emission. This morphology is expected from the projection of a torus of dense gas surrounding the core center (see Fig. 5). We interpret this double-peaked feature as a rotating torus with the blueshifted emission lying predominantly to the north and the redshifted emission lying to the south as indicated by fits to the spectra and the features of the first-moment map. We do not have sufficient resolution in our N_2H^+ $J = 1-0$ spectra to separate out all the hyperfine splitting (HFS) components in the spectra. The presence of the HFS structure complicates the interpretation of the velocity field from the line emission, which can be alleviated by using the isolated component. The moment map is taken over the isolated line component of N_2H^+ $J = 1-0$ F_1 $F = 0, 1 \rightarrow 1, 2$ at a velocity offset by -8.0064 km s^{-1} from the central line (Dore et al. 2004). The velocity range over which the moments are taken is 1.57 km s^{-1} (10 channels).

The moment map of N_2H^+ shows the same extensions to the east and northwest as the integrated intensity map shown in Figure 3*a*. Both the eastern extensions detected in N_2H^+ are redshifted compared to the adjacent gas, with the south eastern one containing the most redshifted gas in the core. The northwestern extension appears blueshifted. A faint extension is detected to the west of the core which could be the southern edge of the cavity created by the redshifted lobe of the outflow.

For comparison, in Figure 9, we show the zeroth-moment map of the FCRAO data alone over the whole mapped area. The B1c source is part of a broader distribution of dense N_2H^+ $J = 1-0$ emission which forms a bridge in emission to the sources to the south: B1a (IRAS 03301+3057) and B1b (Hirano et al. 1997). The distribution is singly peaked, not surprisingly at the position of the brightest peak detected in the BIMA and combined maps, as shown in Figure 9 through images of the BIMA array data and combined data convolved to the FCRAO beam size of 57″.5. We note that the N_2H^+ emission is comparable in extent to the 850 μm SCUBA continuum scale of the core (diameter =1′.6; Kirk et al. 2006). In contrast, BIMA emission alone is tracing scales <1′.3.

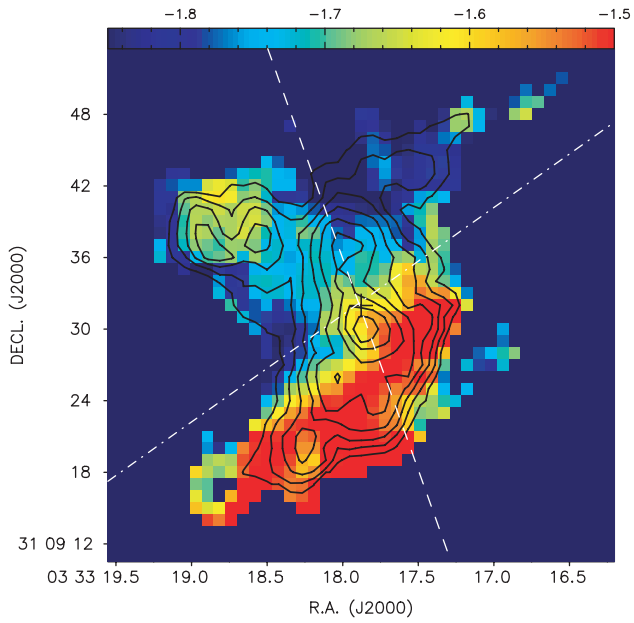

FIG. 8.—First (*gray scale*) and zeroth (*contour*) moment maps from the combined FCRAO and BIMA array observations of N_2H^+ 1–0 emission. The contours are intervals of 0.5 σ from 1.5 to 6 σ, where $\sigma = 0.115$ Jy beam^{-1} km s^{-1}. The cross marks the position of the continuum peak. These maps are taken over the single isolated component of the N_2H^+ hyperfine transitions, F_1 $F = 0, 1 \rightarrow 1, 2$. The white dashed line represents the slice taken to produce the P-V diagram of Fig. 11, and defines the orientation of the "torus" at 10° east of north. The dot-dashed line represents the position angle of the outflow (−55° east of north) as measured from IRAC 4.5 μm and BIMA ^{12}CO $J = 1-0$ data (see § 4.2).

The axis of rotation of the combined map of Figure 8 lies at $\sim -45°$ east of north, which is close to the $-55°$ orientation angle of the outflow (see § 4.2), indicated by the dot-dashed line. However, the axis of rotation is not orthogonal to the plane of the N_2H^+ peaks, which lies at $\sim 10°$ and is indicated in Figure 8 by a dashed line. The offset between the plane of a potential torus (as estimated from the double peaks) and the rotation axis as derived from the first-moment map is 55°, not 90°, as might be expected. Similarly, the offset between the torus and the outflow axis is apparently 65°.

The absence of N_2H^+ emission along the outflow axis is likely due to the carving out of a cavity by the jet associated with the outflow. The combined FCRAO and BIMA zeroth-moment maps of N_2H^+ and HCO^+, shown in Figure 10, mirror the morphology observed in the BIMA data alone. The outflow emission traced by HCO^+ $J = 1-0$ neatly fills the cavity in the N_2H^+ emission. The most strongly blueshifted emission of HCO^+ does not lie at the largest distances from the central source. Similar to Figure 6, there is evidence for redshifted emission at the edge of the blue lobe; the outer edge is certainly less blueshifted than the material closer to B1c.

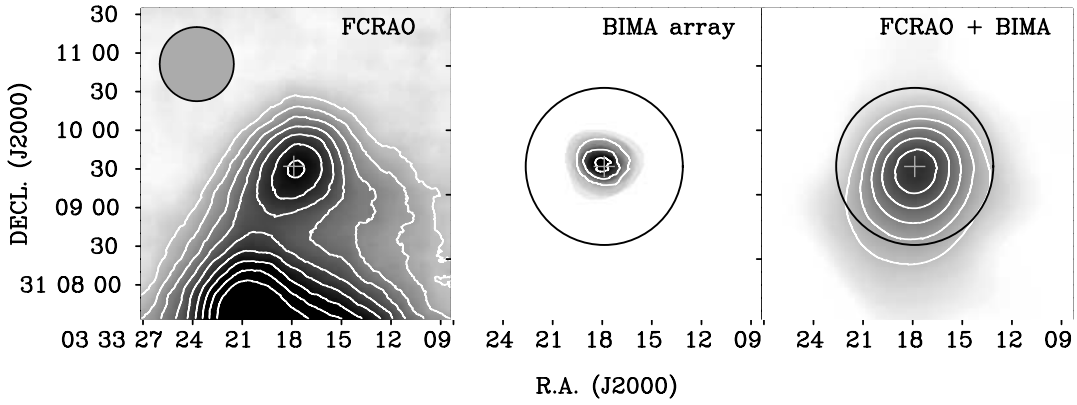

FIG. 9.—Comparison of the zeroth-moment N_2H^+ $J = 1-0$ emission on large scales from FCRAO, the BIMA array, and combined FCRAO and BIMA array data, where the latter two maps have been convolved to the FCRAO beam size of 57″.5, shown at the top left of the FCRAO image. These maps are taken over all seven hyperfine components. The contours of the FCRAO and combined maps are at intervals of 10 σ from 20 to 100 σ, where $\sigma = 1.7$ Jy beam^{-1} km s^{-1}. The BIMA array map has substantially less flux than either the FCRAO or combined maps. The contours plotted range from 4 to 12 Jy beam^{-1} km s^{-1}, in steps of 4 Jy beam^{-1} km s^{-1}. A cross marks the position of the 3 mm source. The BIMA array data, convolved to a similar beam, peaks at the same position as the FCRAO data alone.

4.5. *Kinematics of the Core and Outflow*

4.5.1. *Position-Velocity Diagrams*

We have taken a position-velocity cut along the plane of the torus (through the continuum peak position and the two N_2H^+ $J = 1-0$ peaks) as shown in Figure 8 using the Karma program KPVSLICE (Gooch 1996). Figure 11 shows the P-V emission of the isolated N_2H^+ $J = 1-0$ component. The emission is continuous across the molecular core, but emission peaks are well separated in velocity space. They are symmetric about the velocity of the source for this HFS component (-1.64 km s^{-1}). The distribution of the emission is very narrow in velocity space, limited to only a few velocity channels. Nonetheless, there is a clear velocity gradient across the core with a discernible shift in the centroid velocity across the two off-center peaks.

Figure 12 shows a position-velocity slice taken along the outflow axis through the continuum peak. The orientation of the slice is shown as a dashed line on Figure 10. The distribution of the outflow in velocity space is relatively confined in the HCO^+ $J = 1-0$ emission (which contains both single-dish and interferometric data). The velocity features are more extensive in the ^{12}CO $J = 1-0$ emission, even though it is limited to the spatial frequencies detectable to the interferometer. The redshifted material seen at the leading edge of the blue lobe is evident in the position-velocity (P-V) diagram and no blueshifted emission is observed at offsets beyond that boundary. The redshifted material is detected only in the ^{12}CO $J = 1-0$ emission. It is not seen in HCO^+ $J = 1-0$, although Figure 10 shows that the strongest blueshifted emission is detected close to B1c. At larger distances from the source, the HCO^+ $J = 1-0$ emission is dominated by velocities closer to that of the source.

4.5.2. *Spectra*

Figure 13 shows the distribution of spectra (spatially binned to an area comparable to the beam size) across the core in the combined FCRAO and BIMA data. Fits to the hyperfine components of the N_2H^+ spectra were done using the CLASS software's `hfs`

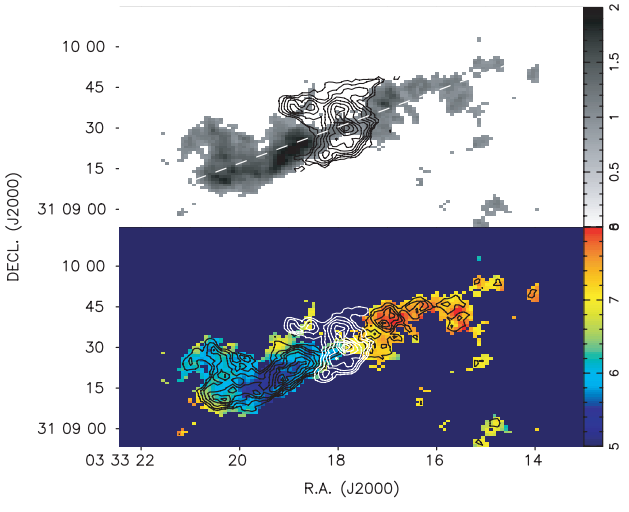

FIG. 10.—*Top panel:* Moment 0 maps of HCO^+ (*gray scale*) and N_2H^+ (*contours*) show the displacement between the HCO^+ and N_2H^+ emission. The HCO^+ emission is confined to a cavity carved into the dense gas by the outflow. Contour levels are 2 to 6 σ in steps of 0.5 σ, where $\sigma = 0.11$ Jy beam^{-1} km s^{-1}. The dashed line shows the position of the position-velocity slice taken through the outflow (see Fig. 12). *Bottom panel:* The first (*gray scale*) and zeroth (*black contours*) moment maps of HCO^+ 1–0 emission from the B1c outflow. In the combined map of FCRAO and BIMA data, the blue lobe of the outflow remains brighter than the red lobe. The white contours show the moment 0 N_2H^+ emission.

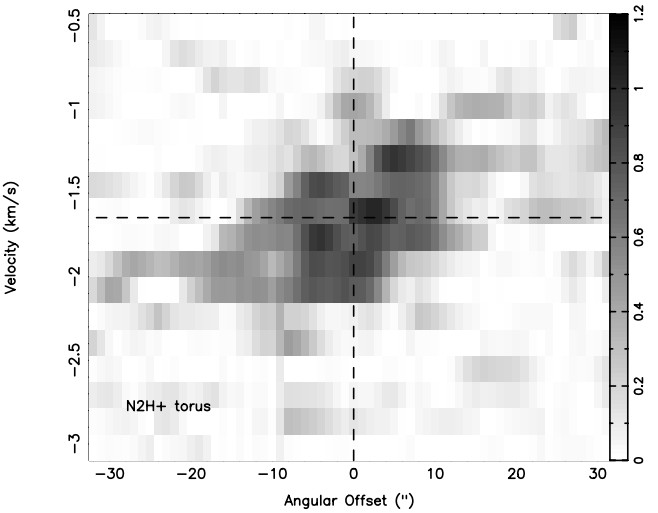

FIG. 11.—P-V diagram of N_2H^+ emission along the plane of the dual peaks observed in the moment map of Fig. 8. Only the isolated component of the hyperfine transitions is used. The central position is coincident with the continuum peak. The systemic velocity of the core for the HFS component is also marked with a dashed line. The velocity gradient across the core is evident.

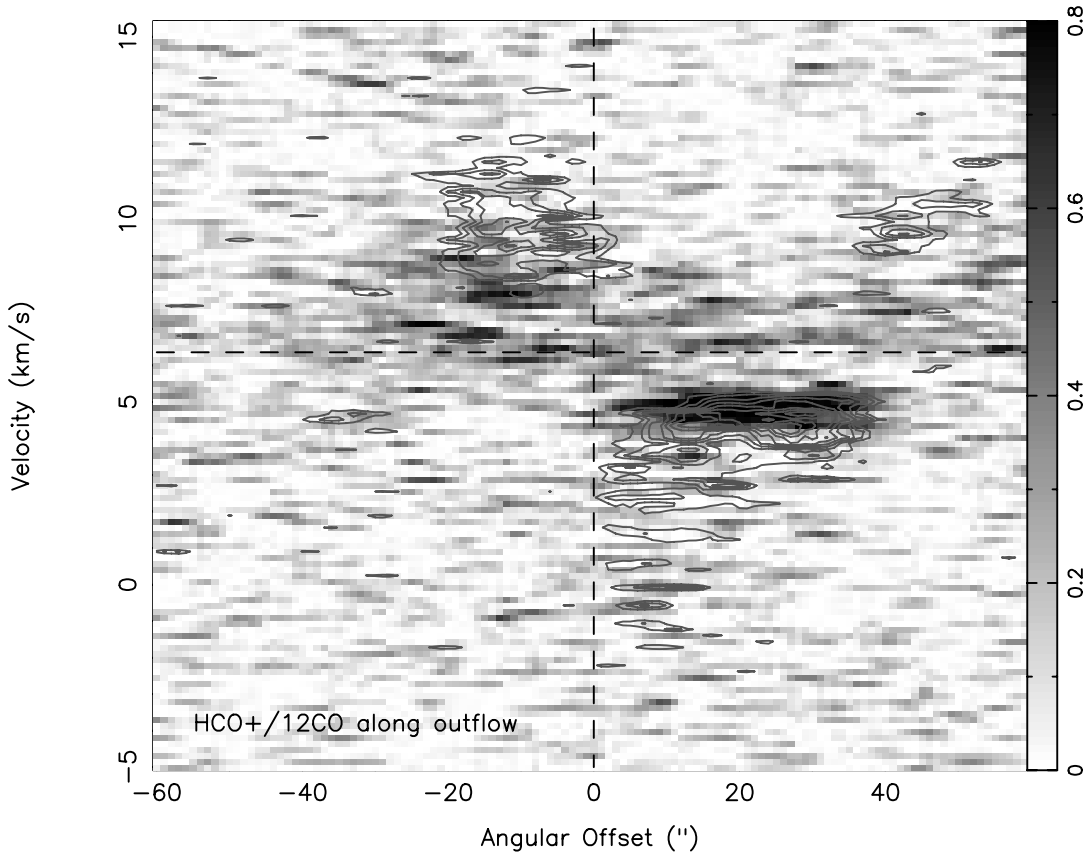

FIG. 12.—P-V diagram of HCO^+ $J = 1–0$ and ^{12}CO $J = 1–0$ emission produced along the outflow axis. The gray scale shows the HCO^+ $J = 1–0$ emission; ^{12}CO $J = 1–0$ emission (BIMA only) is shown in contours of 20 to 90 percentile in steps of 10%. The slice is centered on the position of the B1c continuum source. The orientation of the slice is indicated on Fig. 10.

fitting routine (Buisson et al. 2002) with up-to-date weights and frequencies (Dore et al. 2004). These fits were used to determine local standard of rest velocities (V_{LSR}), intrinsic line widths (Δv), total optical depths [τ(tot)], and excitation temperatures (T_{ex}). The distribution of line strengths is very atypical for N_2H^+. The hyperfine ratio suggests that the central velocity components should be strongest when compared to higher and lower clusters of hyperfine components. In B1c, the central component is often the same strength as the higher velocity component, which is indicative of high opacity or self-absorption of the brightest component. Solutions to the HFS fitting were not substantially improved by using only the outer triplet and the isolated component of the seven hyperfine lines to produce fits to the data for the LSR velocity and the line width; therefore, the fits shown in Figure 13 are all for the fits derived with all seven components.

All seven hyperfine components from the combined data were fit simultaneously in CLASS. We spatially binned the data onto a grid with spacing 5″ in R.A., and 6″ in declination. The fits reflect centroid velocities ranging from 5.94 to 6.68 km s^{-1}. The range of realistic line widths (FWHM) is ~0.3 to 1.5 km s^{-1}. The source velocities are systematically bluer to the north and redder to the south as has been discussed in § 4.4.

Figure 14 shows the distribution of V_{LSR}, ΔV and line opacity (sum of the peak optical depths for all seven hyperfine components) across the core on the same grid as shown in Figure 13. The gradient in V_{LSR} is well defined across the field. Higher values of ΔV are observed along the outflow axis where the cavity has been carved in N_2H^+ emission than across the central core where line widths are quite uniform. Some of the best-fit solutions (assuming a single excitation temperature for all components) shown in Figure 13 produce very large total optical depths for the northern and southern emission peaks. These values indicate that at least one component is very optically thick and all components may be optically thick. We summarize the derived mean, rms, and minimum and maximum values for V_{lsr}, ΔV, and τ(tot) in Table 4. Attempts to fit the spectra with lower, fixed estimates of τ(tot) do an increasingly poor job of fitting the heights of the components. The software's minimum measurable optical depth is 0.1; in these instances, the emission must be optically thin, but we cannot discriminate between values of τ(tot) lower than 0.1. The maximum value yielded is 30, obtained when components have equal strength.

Figure 15 shows only the isolated component of the N_2H^+ spectra, with a velocity range limited to −4 to 0 km s^{-1}. These spectra reveal differences both in the peak of the lines and in line shape across the core, with some positions exhibiting a dip in the center of the line profile, which could indicate that even this line may be optically thick. It is also obvious that regions of poorer S/N produce poorer fits and higher (likely unphysical) estimates of τ.

5. DISCUSSION

5.1. *Column Density and Chemistry*

5.1.1. *Column Density of* N_2H^+

In order to estimate the N_2H^+ column density, we require estimates of the FWHM of the lines and estimates of the line opacity. Figure 14 shows the distribution of line widths and

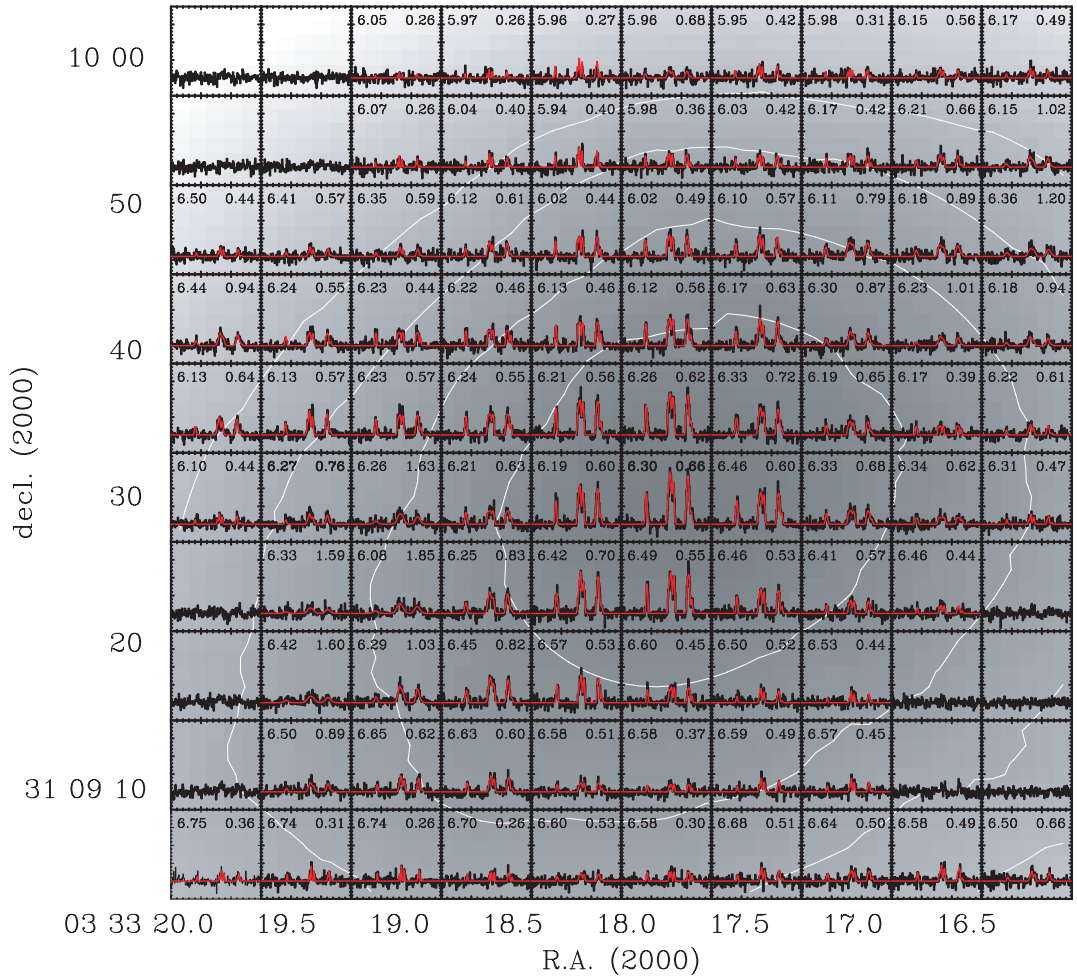

FIG. 13.—N_2H^+ spectra across the B1c inner core. The spectra are integrated across the core in grids of $5'' \times 6''$, which is slightly greater than the beam area. Therefore, the spectra are independently sampling the kinematics of the core. The velocity range is -10 to 20 km s^{-1}, and the intensity range is -0.5 to 2 Jy beam^{-1}. Contours of the moment 0 map are plotted below the spectra. Contours range from 0.35 to 0.91 Jy beam^{-1} km s^{-1} in steps of 0.14 Jy beam^{-1} km s^{-1}. The red lines show the fits to the spectra from CLASS and the fitted values for V_{LSR} and ΔV are shown at the left and right corners, respectively, of each grid square.

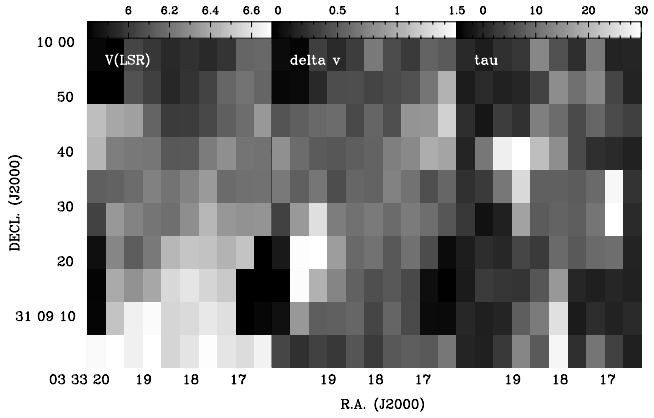

FIG. 14.—Distribution of derived values of V_{LSR}, line width, and total optical depth based on the fits shown in Fig. 13. The gradient across the source is obvious in the derived values of V_{LSR}. The line widths are broader along the direction of the outflow and are narrower along the plane of the torus detected in integrated intensity. The optical depths show a large range of values from optically thin to very optically thick ($\gg 1$), indicating that several HFS components may be optically thick. Table 4 shows the mean values of the parameters derived from the fits to Fig. 13.

opacities derived from the N_2H^+ $J = 1-0$ spectra. We derived the N_2H^+ column density using a simple curve of growth determined by assuming LTE excitation conditions at $T_{ex} = 12$ K, a line width of 0.75 km s^{-1}, and the RADEX escape probability code[3] (Schöier et al. 2005). This simple approach takes into account line opacity, but a more detailed envelope model with proper density and temperature slope will be required to get more accurate estimates (B. C. Matthews et al. 2007, in preparation). Figure 16 shows the column density distribution of N_2H^+ $J = 1-0$ emission in B1c. Since the LTE analysis predicts opacities on the

[3] See http://www.strw.leidenuniv.nl/~moldata.

TABLE 4
PARAMETERS DERIVED FROM N_2H^+ HFS FITTING

Parameter	Mean	rms	Minimum	Maximum
V_{lsr} (km s^{-1})	6.31	2.34	5.94	6.75
ΔV (km s^{-1})	0.61	0.37	0.26	1.85
[a]τ(tot)	6.99	8.37	0.100	30.0

[a] The maximum and minimum solutions for τ(tot) based on the hfs routine are 0.1 and 30, respectively. Values of 0.1 indicate all components are optically thin, while 30 indicates that the component strengths are equal.

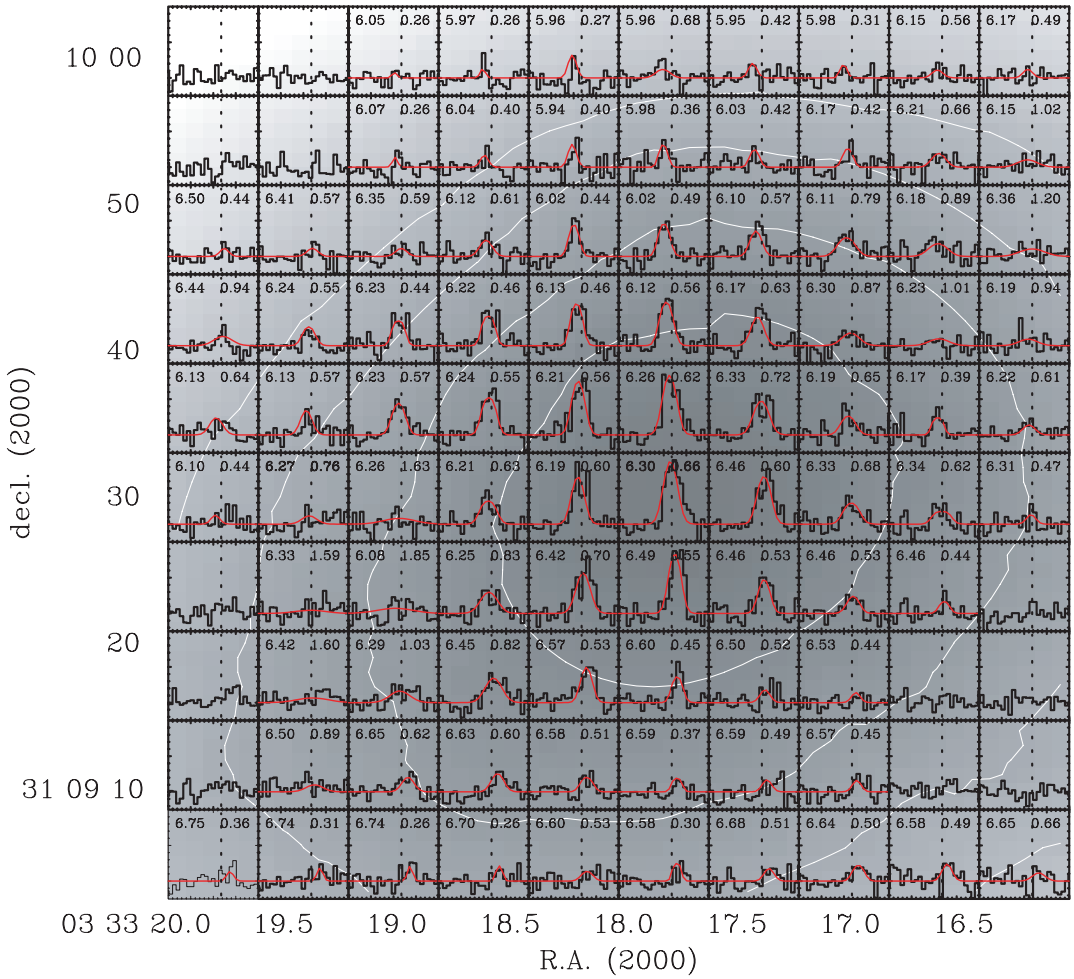

FIG. 15.—N_2H^+ spectra of the isolated hyperfine component of N_2H^+ across the B1c core. The spectra are integrated across the core in grids of $5'' \times 6''$, which is slightly greater than BW sampling. The velocity range is -4 to 0 km s^{-1}, and the intensity range is -0.25 to 1 Jy beam^{-1}. Contours of the moment 0 map are plotted below the spectra. Contours range from 0.35 to 0.91 Jy beam^{-1} km s^{-1} in steps of 0.14 Jy beam^{-1} km s^{-1}. The fits shown as red lines are derived using CLASS for all seven hyperfine components (Fig. 13). The fitted values for V_{LSR} and ΔV are shown at the left and right corners, respectively, of each grid square.

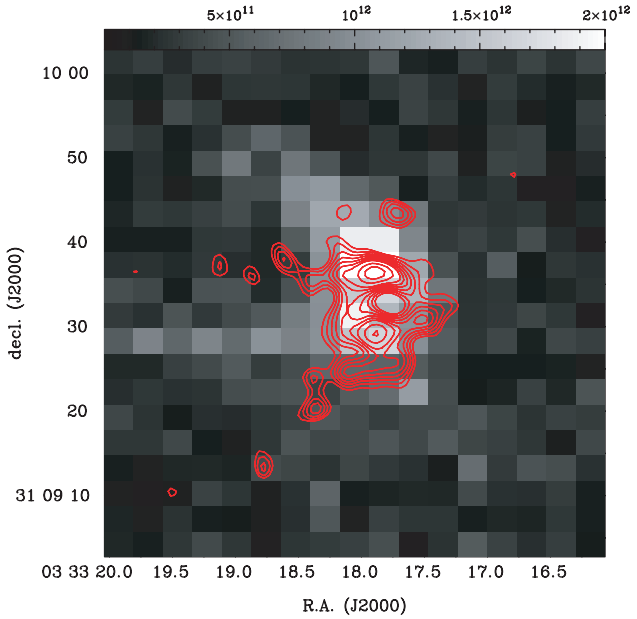

FIG. 16.—Column density distribution of N_2H^+ $J = 1$–0 emission in B1c. Contours are the sum of the N_2H^+ $J = 1$–0 emission over all channels with signal exceeding 3 times the rms level.

order of unity while the spectra and HFS component fitting suggest significantly higher opacities, it is likely that the excitation is not in LTE (i.e., $T_{ex} < 12$ K). However, Figure 16 is illustrative as it shows the same depression in N_2H^+ emission seen in the zeroth-moment map of Figure 17.

5.1.2. *Column Density of* $C^{18}O$

To derive the density at the core center, we estimate the column density at the peak of $C^{18}O$ $J = 1$–0 emission. We can derive the column density from the expression

$$N_{C^{18}O} = \frac{3.34 \times 10^{14}}{\nu\mu^2[1 - \exp(-h\nu/kT_{ex})]} \times \frac{\int T_{MB} dV}{\exp(-Jh\nu/2kT_{ex})} \frac{\tau}{1 - \exp(-\tau)}, \quad (3)$$

where ν is the frequency in GHz (109.78217 GHz), μ is the dipole moment in Debye (0.11 Db), T_{ex} is the excitation temperature, and J is the lower rotational level for the transition. We assume $T_{kin} = T_{ex}$, which is constant for all rotational levels, LTE is valid for the $C^{18}O$ gas and that the optical depth effects are completely accounted for by the factor $\tau/(1 - e^{-\tau})$. We evaluate the integral over the line width from the peak of the moment

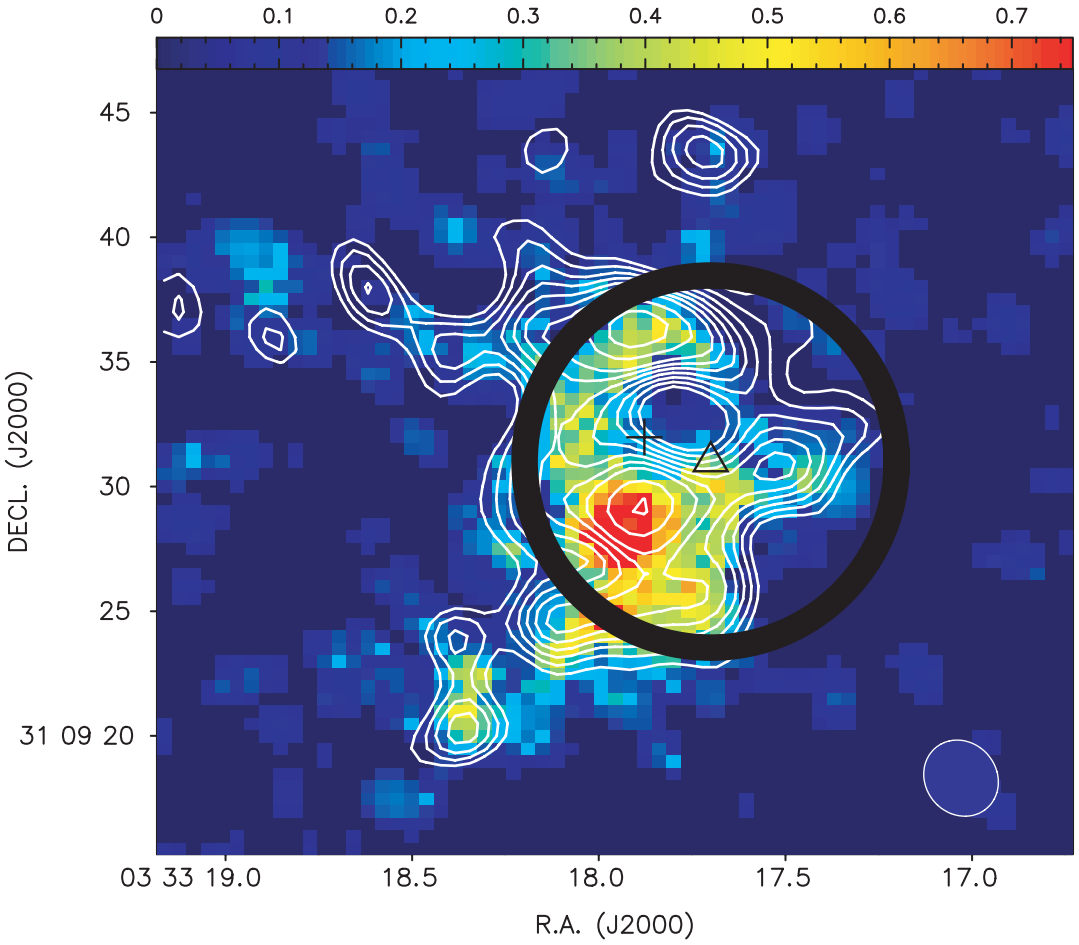

FIG. 17.—Moment 0 map of the N_2H^+ emission from B1c with uniform weighting. The new resolution is $3''.09 \times 2''.52$, almost a factor of 2 improved over the data in § 4.4. The cavity can now be seen as an absence of N_2H^+ emission offset to the west of the continuum peak, marked by a cross. The triangle marks the position of the source as determined from the SCUBA data; the ring depicts the JCMT beam of $14''$. Contours are the same as in Fig. 16.

0 map, integrated over a line width of 1 km s^{-1}. We estimate τ from the peak temperature of the line via the expression

$$T_{\rm peak} \approx \frac{h\nu}{k} \frac{1 - \exp(-\tau)}{\exp(h\nu/kT_{\rm kin} - 1)}, \quad (4)$$

where $T_{\rm kin}$ is the kinetic temperature. From the spectrum at the peak position, we evaluate τ for $T_{\rm peak} = 2$ K and $T_{\rm kin} \approx T_{\rm ex} = 12$ K. We find $\tau = 0.244$, which is consistent with the $C^{18}O$ emission being optically thin. The strength of the emission at the peak is 1.16 Jy beam^{-1} km s^{-1}. Using the conversion factor for our BIMA array synthesized beam at 109 GHz (1.12 K Jy beam^{-1}), $\int T_{\rm MB}\, dV$ is 1.3 K km s^{-1}. Substitution of these values in equation (3) yields a column density of 1.03×10^{15} cm^{-2} (the uncertainty, based largely on the flux calibration, is ~30%). Utilizing the abundance ratio $[C^{18}O]/[H_2] = 1.7 \times 10^{-7}$ (Frerking et al. 1982) yields an H_2 column density of 1.75×10^{22} cm^{-2}. The effective radius of the beam in the $C^{18}O$ observation is 1.8×10^{16} cm. Assuming the core is as deep as it is wide, the density at the peak is $\sim 9.5 \times 10^5$ cm^{-3}. This value is 3 times the estimated central density of 3.2×10^5 cm^{-3} from the analysis of dust emission maps by Kirk et al. (2006) but a magnitude less than the estimate based on 3.3 mm continuum data in § 3.1. The difference is partly attributable to the different spatial filtering between the observations. The 2.7 mm data, with more comparable (u, v) coverage to the $C^{18}O$ data, yields densities of $(3.3 \pm 1.0) \times 10^6$ cm^{-3}, closer to the value derived above.

Aside from the uncertainties introduced by the different degrees of spatial filtering, the discrepancy between the H_2 column density measured with dust and $C^{18}O$ most likely arises due to depletion from standard ISM abundances, leading to underestimates of $N(H_2)$. Although the grains must be heated in B1c due to the centrally peaked distribution of $C^{18}O$, some of the gas could remain frozen onto the dust grains. Assuming the dust represents the total column of the inner envelope and the gas is depleted, then the $[C^{18}O]/[H_2]$ ratio is not 1.7×10^{-7} but instead 1.3×10^{-8} (from 2.7 mm dust continuum), a factor of 13 less. This value is similar to the values measured in Class 0 sources by Jørgensen et al. (2002).

5.2. *A Depression in* N_2H^+ *Emission near the Core Center*

As demonstrated by the integrated intensity and moment maps, the N_2H^+ emission is diminished near the core's center. We are able to produce a more coherent picture of the central "cavity" in N_2H^+ emission by reweighting the N_2H^+ data presented in Figure 8 to uniform when creating the maps. The downweighting of shorter baselines degrades the S/N of the individual channels significantly, but the moment map produced retains high signal by utilizing all seven hyperfine components. Figure 17 shows the moment 0 map produced from the uniformly weighted BIMA array data combined with FCRAO data. A high threshold (3 σ) was placed on inclusion of individual channels into the moment map to avoid channels between components. The cross marks the position of the continuum source, and the triangle represents the

pointing center of the JCMT observations presented in Matthews & Wilson (2002). The ring depicts the 14″ beam of the JCMT. The scale of the evaporated cavity is such that it would not have been resolved by the JCMT. The scale of the cavity is $2\farcs7 \times 2\farcs15$, at a position angle of 7°. This corresponds to 675×540 AU at a distance of 250 pc.

The depression of N_2H^+ emission in the inner envelope and along the outflow path is likely due to the destruction of N_2H^+ by molecules that are released from grains, most notably CO and H_2O. Chemical models of an evolving core with a central luminosity source (i.e., Class 0) suggest that by 10^5 yr a cavity of ~700 AU will be seen in the N_2H^+ abundance and emission (Lee et al. 2004). This is the direct result of stellar heating providing enough energy to evaporate CO from grains within the core center. This model may not be directly applicable to B1c due to differences in masses and/or luminosity, but it provides a rough estimate of the time that has passed since stellar ignition. In addition, observations and models suggest that N_2H^+ will also be destroyed within the outflow (Bachiller et al. 2001; Bergin et al. 1998), and we see a strong anticorrelation between the position of the outflow and the presence of N_2H^+ emission.

A central depression in N_2H^+ emission has also been detected in the transition Class 0/I source L483 by Jørgensen (2004) and in the low-luminosity object IRAM 04191 by Belloche & André (2004). Lee et al. (2005) estimate the inner edge of the IRAM 04191 cavity has a mean radius of 1400 AU. This is a factor of 4 times larger than the cavity detected in B1c. In a simple model where cavities grow over time, this suggests that B1c could be even younger than IRAM 04191's estimated age of 3×10^4 yr since the onset of accretion (André et al. 1999). The gradients and line widths measured in N_2H^+ $J = 1-0$ are strikingly similar in these two cores, indicating strong dynamical similarities, although we stress that IRAM 04191 is one of the new class of very low luminosity objects (VeLLOs; Di Francesco et al. 2006; Young et al. 2004), while B1c is a relatively luminous ($4 \pm 2\ L_\odot$) Class 0 object (B. C. Matthews et al. 2007, in preparation).

We can estimate a kinematic age for this source based on the outflow data. The projected linear extent of the emission coupled with the distance from the source yields estimates of the source age. Using the brightest peak of the blue lobe detected in ^{12}CO $J = 1-0$ and assuming an inclination angle of 45°, the dynamical age is 3.7×10^4 yr, comparable to that of the source IRAM 04191 in Taurus (3×10^4 yr). To produce an age on the order of 10^5 yr, the outflow inclination angle must be ~15° (i.e., the outflow must lie almost along the line of sight).

The absence of N_2H^+ in IRAM 04191 is attributed to depletion within the cold core interior (Belloche et al. 2002). The strong centrally peaked detection of $C^{18}O$ $J = 1-0$ emission from B1c (see Fig. 6) shows that depletion is not significant in B1c, and the anticorrelation between N_2H^+ with the core center and outflow lobes suggests that N_2H^+ is absent due to destruction by CO. In addition, the strong outflow detected with *Spitzer* (Fig. 7) is highly collimated, suggestive of a young source, but its spatial extent suggests that the collapse of the driving source may not have been as recent as that in IRAM 04191. These characteristics are similar to those of L483 which is thought to be in transition to a Class I object (Tafalla et al. 2000).

Lee et al. (2005) note that the centers of the molecular outflow and envelope surrounding IRAM 04191 are offset from the continuum source by approximately 560 AU. They suggest that the two cavities seen to the south of that source could be due to a binary in which one companion is too young to have any appreciable dust emission. There is also evidence for binarity within B1c, particularly in the behavior of its outflow (§ 4.2), which shows evidence of precession. The cavity center is also offset from the continuum source position. There is as yet no detection of a second dust peak nor a second outflow in B1c.

5.3. *Rotational Support*

The observed global rotation velocities within the B1 cloud are insufficient to support the cloud against collapse by a factor of ~8 (Bachiller et al. 1990). The ages of embedded but optically visible objects LkHα 327 and LkHα 328 are between $(4-6) \times 10^6$ yr (Cohen & Kuhi 1979). Based on this, Bachiller et al. (1990) conclude that another mechanism must be providing substantial support to the B1 cloud. Within B1c, the two peaks of the rotating torus can be used to derive the rotational energy relative to the $V_{\rm LSR}$ at the core center of B1c itself.

The inner edges of the torus are offset from the position of the continuum peak. For a sphere, the rotational energy is given by

$$E_{\rm rot} = \frac{2}{5}\rho V v_r^2, \tag{5}$$

where ρ is the mean density, V is the volume, and v_r is the radial velocity relative to the center. Based on estimates of the central density with $C^{18}O$ (§ 5.1.2) and dust emission (Kirk et al. 2006), we adopt a mean density of 5×10^5 cm^{-3} for B1c.

The radial velocity of the two peaks relative each other is ~0.06 km s^{-1} (as derived from Fig. 13). Thus, we estimate the radial velocity relative to the core center to be a relatively small shift of ~0.03 km s^{-1}. The mean offset of the peaks from the core's velocity center is ~4″, or 1000 AU (for $d = 250$ pc), encompassing a volume of 1.4×10^{49} cm^3. Thus, based on equation (5), the rotational energy of the core is $\sim 1.2 \times 10^{39}$ ergs.

Matthews & Wilson (2002) derived the energetics of the B1c core based on estimates of the magnetic field dispersion and found rough equipartition between the gravitational, kinetic, and magnetic energies (all $\sim 10^{48}$ ergs). The rotational energy is thus likely negligible to the support of the core compared to the other means of support available through nonthermal gas motions and magnetic field support.

The radius of the torus (~1000 AU) detected in B1c leads naturally to a discussion of a "pseudodisk" (Galli & Shu 1993) around the protostar within this core. Such a disk is magnetically supported and grows with time. Matthews & Wilson (2002) estimated the magnetic field strength in the low-density regime around the B1 cores to be on the order of 30 μG. While the field strength within the B1c core may be higher, there is no Zeeman splitting measurement of sufficient spatial resolution to isolate the field strength of the individual cores within B1. Assuming the presence of a pseudodisk as described by Galli & Shu (1993) we can use their equation (24) to estimate the age of the disk around B1c. For a field strength of 30 μG and a sound speed of 0.35 km s^{-1}, a disk of radius 1000 AU has an age of 1.8×10^5 yr, consistent with the expected age of a Class 0 protostar.

6. SUMMARY

Utilizing interferometric and single-dish millimeter data from the BIMA array and FCRAO, we have probed the structure of the envelope of the source Barnard 1c in Perseus. We detect a powerful molecular outflow in ^{12}CO $J = 1-0$ and HCO^+ $J = 1-0$, which has carved a conical cavity into the envelope of B1c, destroying N_2H^+. The prominence of the outflow driven by this source is also evident in *Spitzer* IRAC data recently published by Jørgensen et al. (2006). Comparison of the CO molecular outflow

and 4.5 μm data reveals that positions of changes in jet direction are mirrored by changes in velocity in the CO emission.

We have detected significant N_2H^+ $J = 1-0$ emission from B1c. Data from FCRAO reveal N_2H^+ emission is of comparable scale to single-dish dust continuum maps. High-resolution data (created by uniform weighting of the BIMA data combined with the FCRAO data) reveal clearly a small cavity in which dense gas has been destroyed, most likely by heating by the outflowing gas. We have detected a gradient in V_{LSR} of N_2H^+ consistent with rotation; moment maps reveal evidence of a rotating torus offset from the continuum peak position. B1c is similar to the more luminous source L483. Both L483 and B1c show $C^{18}O$ toward the source peak and an anticorrelation of $C^{18}O$ with N_2H^+, indicating that the interior is warm and that CO has been desorbed from grains in that core interiors.

Based on the 3.3 mm dust continuum emission, we estimate that the mass of the B1c inner envelope is in the range of 2.1–2.9 $M_\odot$. This is consistent with the mass of 2.4 $M_\odot$ derived from the JCMT observations (Kirk et al. 2006) for a mean dust temperature of 15 K. However, the 3.3 mm measurement is only an estimate of the inner envelope due to the spatial filtering of the BIMA array data.

It is interesting to note that this core exhibits many features of the standard picture for an evolving young stellar object. In continuum dust emission, the core has a dense centrally peaked interior. However, the N_2H^+ $J = 1-0$ emission appears elongated along an orientation roughly orthogonal to its outflow. The two N_2H^+ peaks suggest the presence of a rotating torus (with $r \sim 1000$ AU) with a central cavity carved out by the outflow and heating by the central source. We argue that the heating has released ^{12}CO and its isotopes from grains near the central source, destroying N_2H^+. N_2H^+ survives in the rest of the inner envelope, as indicated by the torus (or pseudodisk) and the N_2H^+ emission, which brackets the outflow as traced in ^{12}CO $J = 1-0$ and HCO^+ $J = 1-0$. As is the case in L483, the double peaks of N_2H^+ (torus) do not lie orthogonal to the outflow orientation. In B1c, the offset is $\sim 65^\circ$.

Existing polarimetry data (Matthews & Wilson 2002), interpreted in the case of a constant field orientation through the core would indicate a magnetic field direction roughly parallel to the outflow orientation. As yet, there is no estimate of the field strength within B1c itself; however, using the estimate from the surrounding B1 cloud (Matthews & Wilson 2002) and the model of Galli & Shu (1993), the source age is estimated to have a lower limit of 1.8×10^5 yr. The dynamical age estimate of 3.7×10^4 yr is highly dependent on the inclination of the outflow.

In our forthcoming paper (B. C. Matthews et al. 2007, in preparation), we will present higher transition observations of ^{12}CO and $C^{18}O$ from the B1c outflow, as well as measurements of the 1.3 mm continuum from the SubMillimeter Array. With existing data and new data from the Infrared Spectrograph (IRS) on *Spitzer*, we will generate the spectral energy distribution and use it to constrain models of $T(r)$ and $\rho(r)$, which was not possible based on the weak continuum detections reported here.

The authors thank an anonymous referee for an insightful and thorough report which improved the quality of the paper substantially. We would like to thank Mark Heyer for obtaining the FCRAO data for us outside the normal proposal process. We thank Paola Caselli for help with the CLASS software and the HFS component fits and James Di Francesco for many helpful discussions. B. C. M.'s research was supported by an NSERC PDF and Berkeley NSF grant 02-28963. The research of M. R. H. was supported by a VIDI grant from the Nederlandse Organisatie voor Wetenschappelijk Onderzoek. The research of J. K. J. was supported by NASA Origins grant NAG 5-13050. E. A. B. acknowledges support from the NSF grant 03-35207. The BIMA array was operated with support from the National Science Foundation under grants AST 02-28963 to UC Berkeley, AST 02-28953 to U. Illinois, and AST 02-28974 to U. Maryland. FCRAO is supported by NSF grant AST 02-28993.

REFERENCES

Aikawa, Y., Herbst, E., Roberts, H., & Caselli, P. 2005, ApJ, 620, 330
André, P., Motte, F., & Bacmann, A. 1999, ApJ, 513, L57
Arce, H. G., & Sargent, A. I. 2006, ApJ, 646, 1070
Bachiller, R., & Cernicharo, J. 1986, A&A, 166, 283
Bachiller, R., Menten, K. M., & del Rio-Alvarez, S. 1990, A&A, 236, 461
Bachiller, R., Pérez Gutiérrez, M., Kumar, M. S. N., & Tafalla, M. 2001, A&A,372, 899
Belikov, A. N., Kharchenko, N. V., Piskunov, A. E., Shilbach, E., & Scholz, R.-D. 2002, A&A, 387, 117
Belloche, A., & André, P. 2004, A&A, 419, L35
Belloche, A., André, Despois, D., & Blinder, S. 2002, A&A, 927, 947
Bergin, E. A., Alves, J., Huard, T., & Lada, C. J. 2002, ApJ, 570, L101
Bergin, E. A., & Langer, W. D. 1997, ApJ, 486, 316
Bergin, E. A., Neufeld, D. A., & Melnick, G. J. 1998, ApJ, 499, 777
Bisschop, S. E., Fraser, H. J., Öberg, K. I., van Dischoek, E. F., & Schlemmer, S. 2006, A&A, 449, 1297
Bontemps, S., André, P., Tereby, S., & Cabrit, S. 1996, A&A, 311, 858
Borgman, J., & Blaauw, A. 1964, Bull. Astron. Inst. Netherlands, 17, 358
Buisson, G., Desbats, L., Duvert, G., Forveille, T., Gras, R., Guilloteau, S., Lucas, R., & Valiron, P. 2002, Continuum and Line Analysis Single-Dish System Manual (IRAM: Grenoble), http://iram.fr/IRAMFR/GILDAS
Cernicharo, J., Bachiller, R., & Duvert, G. 1985, A&A, 149, 273
Černis, K. 1990, Ap&SS, 166, 315
Černis, K., & Straizys, V. 2003, Baltic Astron., 2, 214
Cohen, M., & Kuhi, L. V. 1979, ApJS, 41, 743
de Zeeuw, P. T., Hoogerwerf, R., & de Bruijne, J. H. J. 1999, AJ, 117, 354
Di Francesco, J., Evans, N. J., II, Caselli, P., Myers, P. C., Shirley, Y., Aikawa, Y., & Tafalla, M. 2006, in Protostars & Planets V, ed. B. Reipurth, D. Jewitt, & K. Kiel (University of Arizona Press: Tucson), in press
Dore, L., Caselli, P., Beninati, S., Bourke, T., Myers, P. C., & Cazzoli, G. 2004, A&A, 413, 1177
Enoch, M. L., et al. 2006, ApJ, 638, 293
Frerking, M. A., Langer, W. D., & Wilson, R. W. 1982, ApJ, 262, 590
Galli, D., & Shu, F. H. 1993, ApJ, 417, 243
Gooch, R. E. 1996, in ASP Conf. Series 101, Astronomical Data Analysis Software and Systems, ed. G. H. Jacoby & J. Barnes (San Francisco: ADP), 80
Herbig, G. H., & Jones, B. F. 1983, AJ, 88, 1040
Hirano, N., Kameya, O., Mikami, H., Saito, S., Umemoto, T., & Yamamoto, S. 1997, ApJ, 478, 631
Hodapp, K. W., Bally, J., Eisöffel, J., & Davis, C. J. 2005, AJ, 129, 1580
Hogerheijde, M. R. 2005, IAU Symp. 231, Astrochemistry Throughout the Universe: Recent Successes and Current Challenges, ed. D. C. Lis, G. A. Blake & E. Herbst (Cambridge: Cambridge Univ. Press), 90
Jørgensen, J. K. 2004, A&A, 424, 589
Jørgensen, J. K., Hogerheijde, M. R., Blake, G. A., van Dishoeck, E. F., Mundy, L. G., & Schöier, F. L. 2004a, A&A, 415, 1021
Jørgensen, J. K., Schöier, F. L., & van Dishoeck, E. F. 2002, A&A, 389, 908
———. 2004b, A&A, 416, 603
Jørgensen, J. K., et al. 2006, ApJ, 645, 1246
Kirk, H., Johnstone, D., & Di Francesco, J. 2006, ApJ, 646, 1009
Lee, C.-F., Ho, P. T. P., & White, S. M. 2005, ApJ, 619, 948
Lee, J.-E., Bergin, E. A., & Evans, N. J. 2004, ApJ, 617, 360
Matthews, B. C. 2005, in ASP Conf. Ser. 343, Astronomical Polarimetry: Current Status and Future Directions, ed. S. Adamson, C. J. Davis, & C. Aspin (San Francisco: ASP), 99
Matthews, B. C., & Wilson, C. D. 2002, ApJ, 574, 822
Noriega-Crespo, A., et al. 2004, ApJS, 154, 352
Öberg, K. I., van Brokhuizen, F., Fraser, H. J., Bisschop, S. E., van Dischoek, E. F., & Schlemmer, S. 2005, ApJ, 621, L33
Ossenkopf, V., & Henning, Th. 1994, A&A, 291, 943
Ridge, N., et al. 2006, AJ, 131, 2921

Sargent, A. I. 1979, ApJ, 233, 163
Sault, R. J., Teuben, P. J., & Wright, M. C. H. 1995, in ASP Conf. Ser. 77, Astronomical Data Analysis Software and Systems IV, ed. R. A. Shaw, H. E. Payne, and J. J. E. Hayes (San Francisco: ASP), 433
Schöier, F. L., van der Tak, F. F. S., van Dishoeck, E. F., & Black, J. H. 2005, A&A, 432, 369
Stanimirovic, S., Staveley-Smith, L., Dickey, J. M., Sault, R. M., & Snowden, L. 1999, MNRAS, 302, 417
Tafalla, M., Myers, P. C., Mardones, D., & Bachiller, R. 2000, A&A, 359, 967
Welch, J. W., et al. 1996, PASP, 108, 93
Whittet, D., Gerakines, P., Hough, J., & Shenoy, S. 2001, ApJ, 547, 872
Whitworth, A. P., & Ward-Thompson, D. 2001, ApJ, 547, 317
Williams, J. P., de Geus, E. J., & Blitz, L. 1994, ApJ, 428, 693
Young, C. H., et al. 2004, ApJS, 154, 396